



HAL
open science

Neoproterozoic atmospheric chemistry and the preservation of S-MIF in sediments from the São Francisco Craton

Alice Bosco-Santos, William Patrick Gilhooly, Paola de Melo-Silva, Fotios Fouskas, Amaury Bouyon, João Gabriel Motta, Mauricio Rigoni Baldim, Wendell Fabricio-Silva, Pascal Philippot, Elson Paiva Oliveira

► To cite this version:

Alice Bosco-Santos, William Patrick Gilhooly, Paola de Melo-Silva, Fotios Fouskas, Amaury Bouyon, et al.. Neoproterozoic atmospheric chemistry and the preservation of S-MIF in sediments from the São Francisco Craton. *Geoscience Frontiers*, 2021, pp.101250. 10.1016/j.gsf.2021.101250 . hal-03264264

HAL Id: hal-03264264

<https://hal.science/hal-03264264>

Submitted on 27 Aug 2021

HAL is a multi-disciplinary open access archive for the deposit and dissemination of scientific research documents, whether they are published or not. The documents may come from teaching and research institutions in France or abroad, or from public or private research centers.

L'archive ouverte pluridisciplinaire **HAL**, est destinée au dépôt et à la diffusion de documents scientifiques de niveau recherche, publiés ou non, émanant des établissements d'enseignement et de recherche français ou étrangers, des laboratoires publics ou privés.



Distributed under a Creative Commons Attribution - NonCommercial - NoDerivatives 4.0 International License



Contents lists available at ScienceDirect

Geoscience Frontiers

journal homepage: www.elsevier.com/locate/gsf

Research Paper

Neoproterozoic atmospheric chemistry and the preservation of S-MIF in sediments from the São Francisco Craton

Alice Bosco-Santos^{a,b,*}, William Patrick Gilhooly III^b, Paola de Melo-Silva^a, Fotios Fouskas^b, Amaury Bouyon^c, João Gabriel Motta^{a,d}, Mauricio Rigoni Baldim^e, Wendell Fabricio-Silva^{f,g}, Pascal Philippot^{c,h,i}, Elson Paiva Oliveira^a

^a Department of Geology and Natural Resources, University of Campinas, Campinas, SP 13083855, Brazil

^b Department of Earth Sciences, Indiana University-Purdue University Indianapolis, Indianapolis, IN, USA

^c Institut de Physique du Globe de Paris, Université de Paris, CNRS-UMR 7154, 75005 Paris Cedex 05, France

^d Vizlab - X-Reality and Geoinformatics Lab, UNISINOS, São Leopoldo, RS 93022-750, Brazil

^e Geosciences Department, Federal University of Mato Grosso, Cuiabá, MT, Brazil

^f Geosciences Institute, University of Brasília, Brasília, Distrito Federal 70910-900, Brazil

^g Institute of Geography and Geology, University of Würzburg, 97074 Würzburg, Germany

^h Géosciences Montpellier, Université de Montpellier, CNRS, Université des Antilles, Montpellier, France

ⁱ Institute of Astronomy, Geophysics, and Atmospheric Sciences, University of São Paulo, Rua do Matão 1226, São Paulo, Brazil

ARTICLE INFO

Article history:

Received 16 September 2020

Revised 14 May 2021

Accepted 4 June 2021

Available online xxx

Keywords:

S-MIF preservation

Archean atmospheric chemistry

GOE

São Francisco Craton

ABSTRACT

Sulfur mass-independent fractionation (S-MIF) preserved in Archean sedimentary pyrite is interpreted to reflect atmospheric chemistry. Small ranges in $\Delta^{33}\text{S}$ that expanded into larger fractionations leading up to the Great Oxygenation Event (GOE; 2.45–2.2 Ga) are disproportionately represented by sequences from the Kaapvaal and Pilbara Cratons. These patterns of S-MIF attenuation and enhancement may differ from the timing and magnitude of minor sulfur isotope fractionations reported from other cratons, thus obscuring local for global sulfur cycling dynamics. By expanding the $\Delta^{33}\text{S}$ record to include the relatively underrepresented São Francisco Craton in Brazil, we suggest that marine biogeochemistry affected S-MIF preservation prior to the GOE. In an early Neoproterozoic sequence (2763–2730 Ma) from the Rio das Velhas Greenstone Belt, we propose that low $\delta^{13}\text{C}_{\text{org}}$ ($< -30\text{‰}$) and dampened $\Delta^{33}\text{S}$ (0.4‰ to -0.7‰) in banded iron formation reflect the marine diagenetic process of anaerobic methane oxidation. The overlying black shale (TOC up to 7.8%) with higher $\delta^{13}\text{C}_{\text{org}}$ (-33.4‰ to -19.2‰) and expanded $\Delta^{33}\text{S}$ ($2.3\text{‰} \pm 0.8\text{‰}$), recorded oxidative sulfur cycling that resulted in enhance preservation of S-MIF input from atmospheric sources of elemental sulfur. The sequence culminates in a metasediment, where concomitant changes to more uniform $\delta^{13}\text{C}_{\text{org}}$ (-30‰ to -25‰), potentially associated with the RuBisCO I enzyme, and near-zero $\Delta^{33}\text{S}$ (-0.04‰ to 0.38‰) is mainly interpreted as evidence for local oxygen production. When placed in the context of other sequences worldwide, the Rio das Velhas helps differentiate the influences of global atmospheric chemistry and local marine diagenesis in Archean biogeochemical processes. Our data suggest that prokaryotic sulfur, iron, and methane cycles might have an underestimated role in pre-GOE sulfur minor isotope records.

© 2021 China University of Geosciences (Beijing) and Peking University. Production and hosting by Elsevier B.V. This is an open access article under the CC BY-NC-ND license (<http://creativecommons.org/licenses/by-nc-nd/4.0/>).

1. Introduction

The first significant increase in atmospheric oxygen concentrations occurred during the Great Oxygenation Event (GOE) from ca. 2.45 to 2.2 billion years ago (Ga) (Holland, 2002). However, controversy remains as to whether it occurred as a rapid step-increase in

oxygen or a long and continuous process that took several hundreds of millions of years before becoming a new stable state of the atmosphere (Bekker et al., 2004; Guo et al., 2009; Reinhard et al., 2013; Luo et al., 2016; Philippot et al., 2018). One of the more robust pieces of evidence for redox change in atmospheric chemistry is the transition from sulfur isotope mass-independent fractionation (S-MIF; where $\Delta^{33}\text{S} \neq 0 \pm 0.2\text{‰}$) to mass-dependent fractionation (S-MDF; where $\Delta^{33}\text{S} = 0 \pm 0.2\text{‰}$) recorded in sedimentary pyrite (Farquhar et al., 2000, 2001).

* Corresponding author at: Department of Geology and Natural Resources, University of Campinas, Campinas, SP 13083855, Brazil.

E-mail address: alicebosco@gmail.com (A. Bosco-Santos).

<https://doi.org/10.1016/j.gsf.2021.101250>

1674-9871/© 2021 China University of Geosciences (Beijing) and Peking University. Production and hosting by Elsevier B.V.

This is an open access article under the CC BY-NC-ND license (<http://creativecommons.org/licenses/by-nc-nd/4.0/>).

The predominance of S-MDF found in pyrite younger than about 2.33 Ga reflects the rise of atmospheric oxygen above 10^{-5} times present atmospheric levels (PAL; Pavlov and Kasting, 2002) and the screening of UV-photolysis of volcanogenic SO_2 at low altitude (Farquhar et al., 2000; Farquhar and Wing, 2003; Ueno, 2014). However, before the global disappearance of S-MIF, a suite of proxies responsive to the presence of free dissolved oxygen or hydrogen sulfide (e.g., iron speciation, Ce anomaly, Mo enrichments, low $\delta^{34}\text{S}$ values, stromatolite fossils) suggest periodic and/or localized oxidative weathering (e.g., Anbar et al., 2007; Kaufman et al., 2007; Reinhard et al., 2009, 2013; Planavsky et al., 2010; Scott et al., 2011; Stüeken et al., 2012; Crowe et al., 2013; Olson et al., 2013; Riding et al., 2014; Zhelezinskaia et al., 2014; Lalonde and Konhauser, 2015). These observations support an emerging view that ocean redox changes were not uncommon before the GOE, at least in semi-restricted or shallow settings, where microbial mats could produce oxygen locally (e.g., Lalonde and Konhauser, 2015).

Although there is consistent evidence for localized oxygen production during the Archean, minor sulfur isotope fractionations ($\Delta^{33}\text{S}$ and $\Delta^{36}\text{S}$) that covary with the carbon isotopic composition of organic carbon ($\delta^{13}\text{C}_{\text{org}}$) are often interpreted as global feedbacks between the biosphere and atmosphere (Domagal-Goldman et al., 2008; Thomazo et al., 2009a, 2009b, 2013; Zerkle et al., 2012). One example is the distinctly small-scale $\Delta^{33}\text{S}$ variations (or dampened S-MIF) observed between 2.9 and 2.7 Ga, which contrast with broader ranges and consistent $\Delta^{36}\text{S}/\Delta^{33}\text{S}$ slope (-0.9), metonymically known as the Archean array, between 2.7 and 2.5 Ga (Ohmoto et al., 2006; Farquhar et al., 2007; Kaufman et al., 2007; Thomazo et al., 2009a, 2013; Zerkle et al., 2012; Kurzweil et al., 2013; Williford et al., 2016). These sulfur isotopic dynamics have been proposed to elucidate microbial feedbacks, specifically methane cycling, that modulated ocean and atmosphere chemistry (Siebert et al., 2005; Anbar et al., 2007; Domagal-Goldman et al., 2008; Thomazo et al., 2009a, 2009b, 2013; Zerkle et al., 2012; Izon et al., 2015).

The interpretations that favor a global biogeochemical influence on the sulfur isotope record before the GOE are potentially spatially biased, particularly for sequences deposited before 2.7 Ga (Fig. 1). Data supporting small-scale $\Delta^{33}\text{S}$ variation before 2.7 Ga are scarce and mainly developed from a limited number of formations in sedimentary sequences from South Africa (Kaapvaal Craton; Farquhar et al., 2007) and Western Australia (Pilbara Craton; Ohmoto et al., 2006; Farquhar et al., 2007; Kaufman et al., 2007; Thomazo et al., 2009a; Marin-Carbonne et al., 2018). Spatially, these observations could represent part of the same contiguous basin of the Vaalbara or Supervaalbara Archean supercontinents (Cheney, 1996; de Kock et al., 2009; Gumsley et al., 2017). If true, other supercratons, such as Superia (North America), Dharwar (India), Zimbabwe (Southern Africa), North China (China), Amazon (Brazil), and São Francisco (Brazil), may never have shared a common history in a single Archean supercontinent (Bleeker, 2003).

Data currently available from these cratons suggest the magnitude of $\Delta^{33}\text{S}$ observed in sedimentary pyrites between 2.8 and 2.5 Ga may be related to Archean paleogeography. The relatively well-studied Kaapvaal (Hu et al., 2003; Kamber and Whitehouse, 2007; Papineau et al., 2007; Guo et al., 2009; Ono et al., 2009a, 2009b; Zerkle et al., 2012; Farquhar et al., 2013; Fischer et al., 2014; Guy et al., 2014), Pilbara (Ono et al., 2003; Ohmoto et al., 2006; Farquhar et al., 2007; Kaufman et al., 2007; Philippot et al., 2007; Partridge et al., 2008; Thomazo et al., 2009a; Gregory et al., 2015; Muller et al., 2016) and Yilgarn (Xue et al., 2013; Chen et al., 2015; Gregory et al., 2016; Caruso et al., 2018) cratons exhibit wide ranges in $\Delta^{33}\text{S}$, from -5% to 11.77% (Fig. 1). In contrast, the $\Delta^{33}\text{S}$ ranges (-3.15% to 4.82%) observed in the Amazon (Fabre et al., 2011; Bühn et al., 2012), São Francisco (Zhelezinskaia

et al., 2014; Bosco-Santos et al., 2020), Dharwar (Mishima et al., 2017; Muller et al., 2017), North China (Hou et al., 2007), Zimbabwe (Hofmann et al., 2009; Thomazo et al., 2013) and Superior (Kurzweil et al., 2013; Hauri et al., 2016; Li et al., 2017) cratons are relatively small (Fig. 1).

We suggest the asynchronous changes in the magnitude of $\Delta^{33}\text{S}$ that occurred on a global scale prior to the GOE (Philippot et al., 2018) could best be attributed to a discrepancy between the formation and preservation mechanisms of S-MIF. An improved representation of the secular record of S-MIF from different terrains is needed to extract a more global framework of the timing and tempo of Earth's surface oxygenation. We fill a gap in this record by providing evidence from an early Neoproterozoic sequence from the São Francisco Craton that shows an attenuation of S-MIF potentially affected by local biogeochemistry. Our interpretation gives a new perspective to differentiating global and local S-MIF dynamics when placed in temporal and geospatial context with sequences from Western Australia and South Africa.

2. Geological background

The São Francisco Craton, located in eastern Brazil, is a large, well-exposed Archean shield, surrounded by Neoproterozoic fold belts (Heilbron et al., 2017). The southern part of the craton represented mainly by the Quadrilátero Ferrífero Province, is characterized by (i) an Archean basement consisting of a series of magmatic complexes of tonalite-trondhjemite-granodiorite (TTG) affinity, generally gneissified or migmatized, (ii) two main Archean metavolcano-sedimentary sequences, represented by the Pitangui and Rio das Velhas Greenstone Belts, (iii) Neoproterozoic granitoids comprising a series of intrusive medium- to high-K calc-alkaline granite stocks and batholiths, and (iv) Neoproterozoic metasedimentary sequences represented mainly by the Minas Supergroup and Bambuí Group (Fig. 2; Renger et al., 1994; Alkmim and Marshak, 1998; Romano, 2006; Teixeira et al., 2015; Marinho et al., 2018; Brando Soares et al., 2020).

In the Quadrilátero Ferrífero region, the gneiss basement corresponds to the Bonfim, Belo Horizonte, Bação, Santa Bárbara and Caeté complexes, exposed as domal structures of fine-grained banded orthogneiss intruded by weakly- to non-foliated younger K-rich granitoids. Four main magmatic events were recognized (Machado and Carneiro, 1992; Lana et al., 2013; Farina et al., 2015; Brando Soares et al., 2020): (i) Santa Barbara, (ii) Rio das Velhas I; (iii) Rio das Velhas II and (iv) Mamona. The initial Santa Barbara event marks the emplacement of the 3.2 Ga TTG gneisses in the Santa Bárbara Complex. The Rio das Velhas I and II events are the most intense periods of crustal formation in the region (2.9–2.7 Ga), including the Bonfim, Belo Horizonte, Bação and Caeté Domes, and Pitangui and Rio das Velhas Greenstone Belts. The Mamona Event (2.7–2.6 Ga) marks the stabilization of the craton with widespread late Neoproterozoic K-rich magmatism. During the ca. 2.77 Ga regional deformation and the metamorphic event caused by orogenesis and crustal thickening, the metamorphic grade of the Rio das Velhas Greenstone Belt ranged from greenschist to amphibolite facies (450–550 °C; Cutts et al., 2019).

The Rio das Velhas Greenstone Belt includes the overlying Maquiné Group and the basal Nova Lima Group (Baltazar and Zucchetti, 2007) (Fig. 2B). The stratigraphy is subdivided into three different tectonostratigraphic blocks: (i) Santa Barbara, (ii) São Bartolomeu, and (iii) Nova Lima-Caeté (Araújo et al., 2020a, 2020b). The rock sequence of the Santa Barbara Block is composed of basal metakomatiites (Quebra Osso Group), followed by tholeiitic metabasalts and clasto-chemical metasedimentary rocks of the Nova Lima Group (Vigário da Vara, Santa Quitéria and Córrego do Sítio formations) and metasedimentary rocks of the Maquiné Group

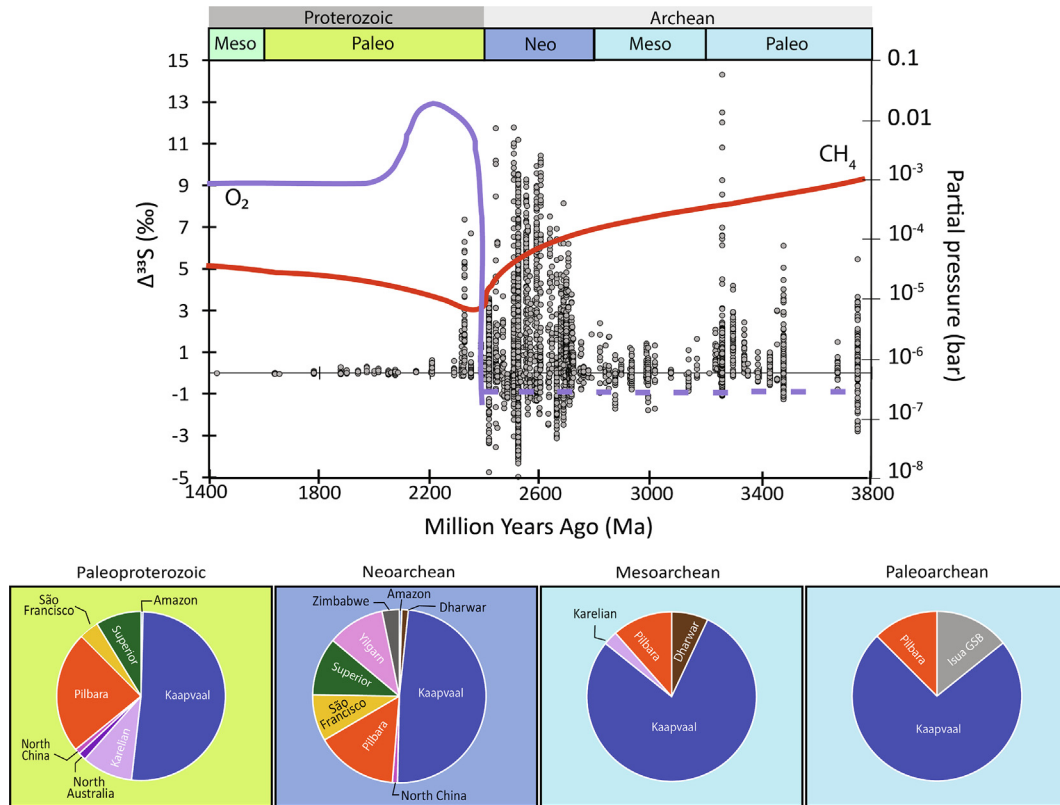


Fig. 1. Compilation of $\Delta^{33}\text{S}$ in sedimentary sulfides (grey circles) and hypothesized partial pressures of O_2 (purple line) and CH_4 (red line) from 1400 to 3800 million years ago (Ma). $\Delta^{33}\text{S}$ in sedimentary sulfides from different terrains (Isua Greenstone Belt terrain, Kaapvaal, Pilbara, Karelian, Dharwar, Amazon, São Francisco, North China, Zimbabwe, North Australia, Superior, and Yilgarn Cratons) are presented by Era from the Paleoproterozoic to the Paleoproterozoic. Data are from several authors as compiled by Selvaraja et al. (2019) and Bosco-Santos et al. (2020).

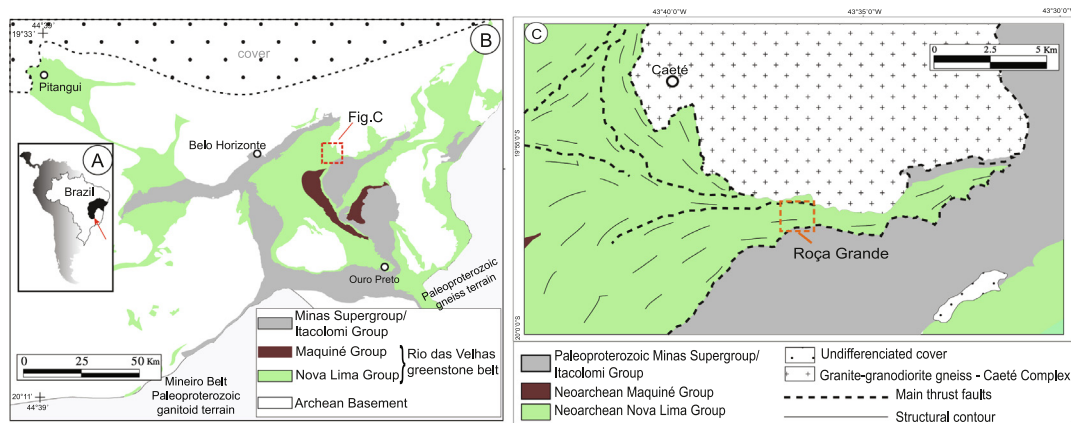
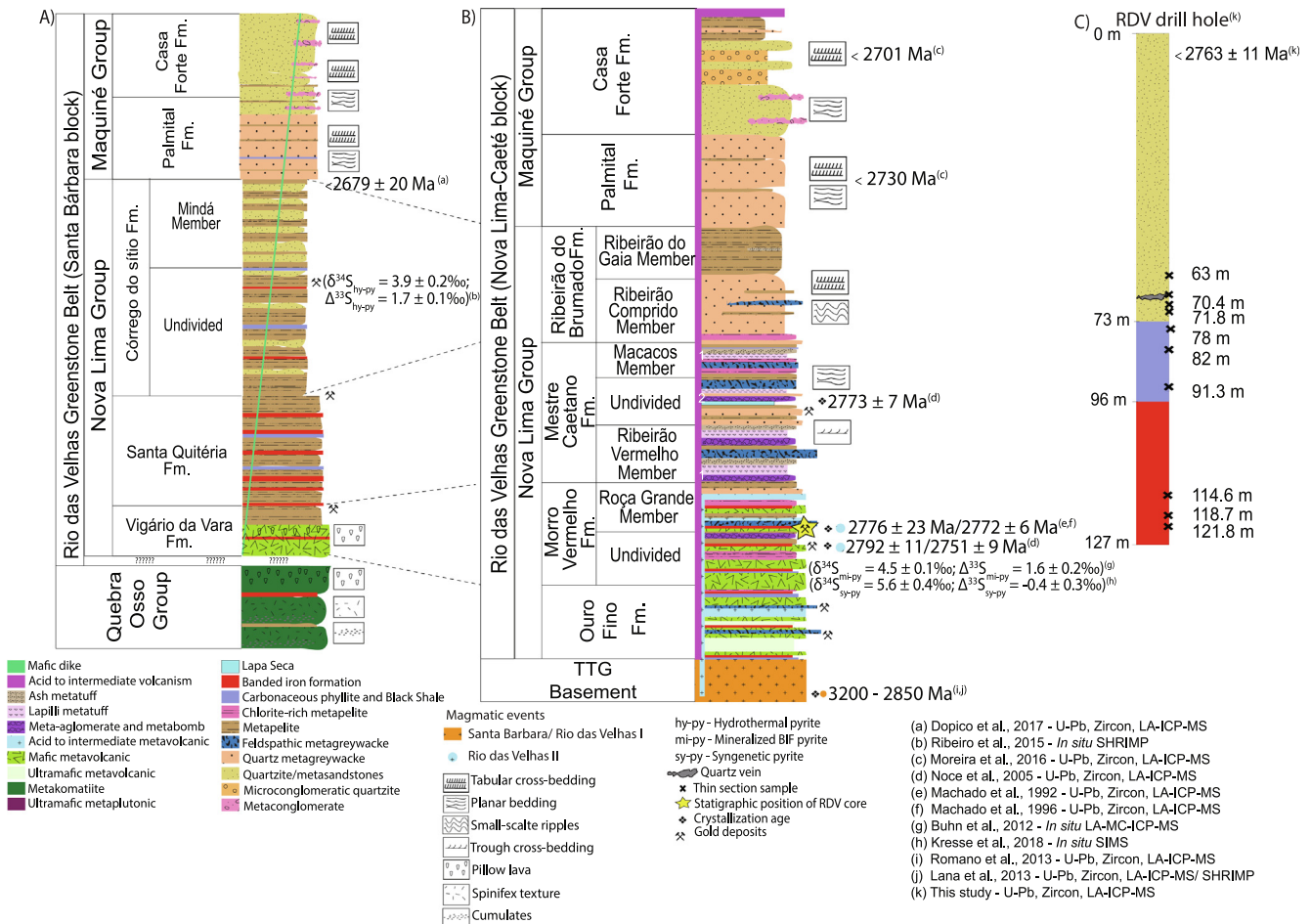


Fig. 2. Study location and geological settings: (A) São Francisco Craton, Brazil. The study area is indicated by the red arrow (in the southern SFC). (B) Main geological domains of the Quadrilátero Ferrífero (adapted from Moreira et al., 2016). (C) Detail of Roça Grande mine location corresponding to the Nova Lima Group, where the samples analyzed and discussed were sampled.

(Palmital and Casa Forte formations; Araújo et al., 2020a). The São Bartolomeu Block contains the metasedimentary rocks of the top of the Nova Lima Group (Fazenda Velha, Córrego da Paina and Pau D'Óleo formations) and a distinct unit of the Maquiné Group (Andaimés Formation; Araújo et al., 2020a). Finally, the Nova Lima-Caeté Block shows a complete greenstone belt sequence. In this block, the basal units of the Nova Lima Group consist of intercalated volcanic rocks of different compositions, volcanoclastic, clastic, and chemical sedimentary rocks of the Ouro Fino and the overlying Morro Vermelho Formation; followed by a sequence of

acid and intermediate metavolcanic and metavolcaniclastic rocks (Mestre Caetano Formation); and a top metasedimentary sequence with a significant volcanogenic contribution (Ribeirão do Brumado Formation). The siliclastic rocks of the Maquiné Group (Palmital and Casa Forte formations) complete the sequence (Fig. 3).

The Roça Grande gold deposit (18 t Au reserve, 2.3 g/t Au grade) is a structurally-controlled banded iron formation (BIF, Vial et al., 2007) from the Morro Vermelho Formation. The lithotypes in the deposit consist of greenschist facies rocks such as chlorite- and carbonaceous schists, with the first corresponding to metavolcanic



rock levels in the footwall, and less-voluminous quartz-sericite schists, quartzose schists, and BIFs towards the hanging wall. The BIFs are interpreted as the Algoma-type, with both magnetite- and carbonate-subtypes (Lobato et al., 2001). These are considered as deposited in a relatively intermediate distance from seafloor hydrothermal fumaroles with restricted detrital input, as evidenced by the low Al and Ti content of chert layers and low Eu anomalies (Araújo and Lobato, 2019). The ore mineralogy is characterized by a preponderance of pyrite and arsenopyrite, with minor marcasite, sphalerite, chalcopyrite, and pyrrhotite (Vial et al., 2007; Araújo and Lobato, 2019). The gangue mineralogy is composed of quartz as veins and chlorite and sericite as matrix alteration. The hydrothermal alteration halo exhibits sulfidation, silicification, chloritization, sericitization, and carbonatization. The alteration is represented by broad linear to widely lenticular ore bodies and envelopes. Localized mineralization associated with saccharoid quartz and sericite exists in shear zone traces with concentrated strain.

The contact between the Morro Vermelho Formation and the underlying Ouro Fino Formation is gradational, with increased contribution of clastic metasedimentary rocks (Araújo et al., 2020a). The Morro Vermelho Formation is subdivided into two members, the topmost Roça Grande Member comprises mainly metasedimentary rocks (Baltazar and Silva, 1996; Baltazar et al., 2005; Araújo et al., 2020a). Its contact with the underlying member, Undivided Morro Vermelho, is transitional. Isotopic U-Pb zircon data in rocks from Morro Vermelho Formation yielded crystallization ages of 2776 ± 23 Ma and 2772 ± 6 Ma for the felsic volcanism

(Machado et al., 1989, 1992; Araújo et al., 2020a), and 2751 ± 9 Ma in metavolcano-clastic greywackes (Noce et al., 2005; Araújo et al., 2020b). These ages are related to the Rio das Velhas II magmatic event, representing the final stage of TTG crust production in the Quadrilátero Ferrífero (Lana et al., 2013; Romano et al., 2013). The youngest maximum depositional age for the overlying Mestre Caetano Formation is 2766 Ma (2773 ± 7 Ma, U-Pb zircon) in metaconglomerate (Noce et al., 2005; Araújo et al., 2020b). The maximum depositional age for the Nova Lima Group's top unit is 2679 ± 20 Ma in detrital zircons within quartzites (Dopico et al., 2017).

The Maquiné Group is composed of near-shore metasandstones and metaconglomerates (Moreira et al., 2016). This group yielded U-Pb zircon maximum depositional ages between 2770 and 2700 Ma, with a maximum depositional age of 2730 Ma in the basal Palmital Formation (Moreira et al., 2016).

3. Materials and methods

3.1. Drill hole sampling and screening

A 127 m of drill hole was sampled inside the Roça Grande gold deposit in collaboration with the Jaguar Mining company and named RDV. The drill hole was sampled in the RG07 mineralized body where gold is hosted in quartz veins within what was described by Jaguar mining as schist (Cox and Pressacco, 2016). Based on petrographic screening described in Section 4.1, the schist was reclassified as a metasandstone. The RG07 mineraliza-

tion host rock is associated with a quartz vein which contrasts with banded iron formation assemblages that host other mineralized bodies in the deposit (Cox and Pressacco, 2016). From bottom to top, three different lithostratigraphic units were identified in the RDV drill hole (Fig. 3): fine-grained carbonate BIF (127–96 m depth); black shale (96–73 m depth); and metasediment (73–0 m depth). The bedding (S_0) is well defined and mostly preserved, superimposed by a schistosity foliation (S_1) and localized crenulation cleavage (S_2) in the most ductile rocks. The section contains a quartz vein emplaced within metasediment (Fig. 3). The quartz vein is narrow (ca. 5 cm) and localized between 68.5 and 69 m. A total of 75 samples (32 from BIF, 20 from black shale, and 23 from metasediment) were selected for geochemical analysis. Each sample consists of a maximum of 10 cm long split cores. For petrographic analysis, polished thin sections were made of 11 hand samples from 3 representative rock types. Samples from BIF were selected from core depths 112 m, 114.6 m, and 119 m, and the black shale samples came from 78 m, 82 m, and 91.3 m. A sample from the quartz vein and three more samples were selected within the metasediment (one above at 63 m depth and two below at 70.4 and 71.8 m).

3.2. U-Pb isotopes in zircon grains

Detrital zircon grains were separated and analyzed for U-Pb age dating by laser ablation sector field inductively coupled plasma mass spectrometry (LA-SF-ICP-MS) at the Isotope Geology Laboratory of the Geosciences Institute of the University of Campinas. Zircon concentrates were extracted from a composite sample of metasediment in the upper ~25 m of the RDV core. Grain separation was made by wet hand panning, magnetic (Frantz), and density separation (heavy liquids) steps before zircon grains were hand-picked under a binocular microscope. The selected grains were mounted on an epoxy disk and polished to obtain a flat surface. The morphology and internal structure of individual grains were imaged by cathodoluminescence to avoid defects, micro-inclusions, and microfractures. The mount was cleaned with HNO_3 and loaded into a laser ablation peripheral (Excite 193, Photon Machines) linked to a single-collector sector field ICP-MS (Element XR, Thermo Scientific) according to the procedures of Navarro et al. (2015). The spot size was set to a diameter of 25 μm . Ultrapure helium was used as the carrier gas, and the laser frequency was 10 Hz with a fluency of 4.74 J cm^{-2} . During the analytical session, forty-six analyses of the 91500 zircon standard (1065 Ma; Wiedenbeck et al., 1995) yielded a pooled mean $^{206}\text{Pb}/^{238}\text{U}$ age of 1060.3 \pm 4.2 Ma. An internal standard (Peixe ID-TIMS, 571 \pm 10 Ma; Navarro et al., 2017) was used to monitor the quality of the reduction procedures. Fifteen Peixe zircon analyses yielded a concordia age of 559.62 \pm 2.69 Ma (MSWD = 2.76). Data reduction was made using Lolite 2.5 software after common Pb correction (performed on VizualAge 2014.10 software; Petrus and Kamber, 2012). Concordia and age histograms were made in Isoplot 4.15 (Ludwig, 2012), and all uncertainties were reported as 2σ values.

3.3. Metamorphic peak temperature

A thin section of black shale sampled from 82 m depth was selected for Raman spectroscopy due to the high content of carbonaceous material observed during petrographic description. Peak temperatures of crystallization were estimated from Raman spectra (Buseck and Beyssac, 2014) of first-order (1000–1800 cm^{-1} ; Henry et al., 2019), disordered (D, 1340–1360 cm^{-1}), graphite (G) (ca. 1580 cm^{-1}), and D2 (ca. 1610 cm^{-1}) bands according to four different calibration curves proposed in the literature (Table 1). For all equations used, the parameters R1 (band height

D1/G) or R2 (band areas D1/(G + D1 + D2)) were calculated, where D corresponds to disordered amorphous organic matter (Beny-Bassez and Rouzaud, 1984) and G is related to the in-plane vibration of carbon atoms in graphene sheets with E2g2 symmetry (Tuinstra and Koenig, 1970; Jehlička and Beny, 1999). In order to account for the potential effects that thin section preparation may influence the D1-band region (Henry et al., 2019), we adopted a range of calibration approaches for a conservative estimate of peak temperature.

3.4. Geochemistry

3.4.1. Major and trace metals

Metal concentrations (Al, Fe, Cr, Ni, Zn, Rb, Sr, Ba, Mo, W, Se, Pb, Bi, Nb, U, Th, Y, REE, and Hf) were measured in bulk rock samples after total acid digestion in the Isotope Geology Laboratory at the University of Campinas. Acid decomposition, evaporation, and recovery were conducted in a microwave reaction system (Multiwave PRO, Anton Paar), equipped with acid digestion (8NXF100) and evaporation rotors (8EVAP). Total digestion in the microwave system was done according to Magaldi et al. (2019), where approximately 100 mg of bulk rock powder was digested with 2 mL of saturated NH_4HF_2 (~63 g/100 mL, 98% metal basis), 2 mL of HNO_3 (65% Merck KgaA) and 2 mL of ultrapure water. Ammonium bifluoride was purified using a 120 mL PFA sub-boiling system (Savillex Corporation, Eden Prairie) heated by a lamp. The HNO_3 was purified in a sub-boiling still (DST-1000 Savillex). Ultrapure water was obtained from a Milli-Q water purification system (Millipore SAS). After digestion, the metals were determined by quadrupole ICP-MS equipped with Collision Cell Technology (XSERIES 2, Thermo Fisher Scientific) calibrated with multi-elemental solutions prepared by mixing the necessary amounts from respective elemental 10 mg/L standards (High Purity Standards, USA). Rhenium was used as an internal standard on conventional mode, and indium was measured in a collision cell. For analytical quality control, we analyzed the certified reference material Green River Shale (SRG-1, USGS). Calculated recovery was generally better than 90% (ranging between 83% and 100%).

The potential mobility of elements resulting from the possible hydrothermal alteration associated with the RDV quartz vein was estimated using the Isocon mass balance method (Grant, 1986; Eq. 1). This method determines the change in the concentration of a component (ΔC_j) using a linear relationship between the concentration of the component (C_j) in altered rock (A) to that of the original (o):

$$\Delta C_j = (M_A/M_o)(C_j^A/C_j^o) - 1 \quad (1)$$

where the ratio between the mass of the altered (M_A) and reference mass of the original, or less altered, sample (M_o) is obtained by the inverse of the Isocon slope best-fit. Components that plot along the linear array are immobile, those that plot above the array are gained, and those that plot below are lost during alteration.

Table 1
Different calibration curves to estimate peak temperature of organic matter maturity using first-order Raman spectra bands.

Reference	Calibration equation = (T °C)	Peak temperature range (°C) (\pm error)
Beyssac et al. (2002)	$-445 \times R2 + 641$	330–640
Rantitsch et al. (2004)	$(-457 \pm 53) \times R2 + (648 \pm 25)$	350–550
Rahl et al. (2005)	$737.3 + 320.9 \times R1 - 1067 \times R2 - 80.638 \times R1^2$	100–700 (± 50)
Aoya et al. (2010)	$91.4 \times R2^2 - 556.3 \times R2 + 676.3$	340–655 (± 30)

In addition to this index of alteration, the relative mobility of trace elements between samples across the core was evaluated according to the relationship of [Ague and Van Haren \(1996\)](#):

$$t_j = [(C_i^0 / C_i^A) (C_j^A / C_j^0) - 1] \quad (2)$$

where mass change for a mobile element (t_j) is represented by the product of concentration ratios (in ppm) of the reference species (C_i) or the mobile species (C_j) for fresh, relatively unaltered rock and altered rock samples. One sample for each lithology that best represents the average chemical composition for that lithology within the core was selected as the least altered reference (7.0 m for metasandstone, 89.2 m for black shale, and 113.6 m for the BIF). In all treatments, zirconium was used as the immobile reference species. Variation in an element between the altered sample and the fresh/less altered sample is considered anomalous when its relative value exceeds $\pm 70\%$ ([Lebrun et al., 2017](#)).

3.4.2. Iron speciation

Iron speciation was conducted in the Stable Isotope Biogeochemistry Laboratory at Indiana University Purdue University Indianapolis according to the methods of [Poulton and Canfield \(2005\)](#). In brief, the sequential extraction procedure isolates the reducible iron and manganese from carbonates (Fe_{Carb}), oxides (Fe_{Oxi}), and magnetite (Fe_{Mag}). Approximately 0.1 g of rock powder was reacted with a solution of sodium acetate (1 M, pH 4.5) for 48 h in a shaker water bath at 50 °C to dissolve the carbonate phase. The sample was centrifuged to concentrate the residue, and the solution containing the Fe_{Carb} fraction was pipetted into a separate vial for quantification. Sodium dithionite (50 g/L, pH 4.8) was added to the residue for 2 h to remove the oxide phases (ferrihydrite, goethite, and hematite). After collecting this fraction, the remaining sample was reacted for 6 h with ammonium oxalate (0.2 M, pH 3.2) to extract magnetite. The iron concentrations in all these phases were measured by Flame Atomic Absorption Spectroscopy (AAS, Perkin Elmer 2380) using a lamp with a 248.3 nm wavelength (Iron, Sci-Tech Corporation). Measurements made in triplicate ($n = 3$, for each fraction) agreed within 10% to 14%.

Pyrite was extracted by chromium reduction ([Canfield et al., 1986](#)). The digestion was performed using boiling 1 M chromous chloride ($CrCl_2$) and concentrated HCl. The hydrogen sulfide evolved during the acid distillation process was trapped in 3% zinc-acetate, then split into a small (1 mL) and a larger (10 mL) aliquot. Sulfide concentrations were measured colorimetrically from the smaller aliquot ([Cline, 1969](#)). The amount of iron in pyrite (Fe_{Py}) was calculated from the sulfide concentrations assuming the stoichiometry of FeS_2 .

Highly reactive iron (Fe_{HR}) was calculated as the sum of Fe_{Carb} , Fe_{Oxi} , Fe_{Mag} , and Fe_{Py} . Unreactive iron (Fe_U) was calculated as the difference between Fe_{HR} and the total iron concentration (Fe_T) measured by ICP-MS after total digestion. The relative distribution of these iron minerals was compared using ratios of Fe_{HR} and Fe_{Py} to Fe_T (Fe_{HR}/Fe_T and Fe_{Py}/Fe_T). These relationships are based on the reactivity of different iron minerals to dissolved sulfide ([Poulton and Canfield, 2005](#)). We also considered that Fe in carbonates and pyrite behaves as a ferrous cation [$Fe(II)$] while Fe bound to oxyhydroxides (goethite and hematite) and magnetite is a ferric cation [$Fe(III)$] ([Johnston et al., 2010](#); [Poulton and Canfield, 2011](#)).

3.4.3. Sulfur isotopes

The sulfide retained in the larger aliquot from the pyrite extraction procedure was precipitated as Ag_2S with a solution of 3% silver nitrate and 10% ammonium hydroxide (wt./volume). The precipitates were dried overnight at 50 °C, then homogenized with agate mortar and pestle for sulfur isotopic analysis. All Ag_2S precipitates were weighed (0.2 mg) into tin cups and combusted to sulfur diox-

ide in an elemental analyzer (Thermo, EAIsolink) coupled under continuous flow to a stable isotope ratio mass spectrometer (Thermo, DeltaV Plus) in the Stable Isotope Biogeochemistry Laboratory at Indiana University-Purdue University Indianapolis. The sulfur isotope composition ($^{34}S/^{32}S$ and $^{33}S/^{32}S$) was measured using the SO-SO₂ collector array and reported relative to Vienna Canyon Diablo Troilite (VCDT) by normalization to three international reference materials ($\delta^{34}S$: IAEA S1 = -0.3% , IAEA S2 = 22.62% , and IAEA S3 = -32.49% ; $\delta^{33}S$: IAEA S1 = -0.05% , IAEA S2 = 11.48% , and IAEA S3 = -16.65% ; [Ding et al., 2001](#)). The results were reported in delta notation in per mil (‰): $\delta^X S = [(^{X-}S/^{32}S_{sample}) / (^{X-}S/^{32}S_{VCDT}) - 1] \times 10^3$, where $X = 33$ or 34 . We presented ^{33}S data as deviations in ‰ from a reference fractionation line using capital delta notation and the mass fraction exponent expected for mass-dependent fractionation (0.515): $\Delta^{33}S = \delta^{33}S - 1000 \times [(1 + \delta^{34}S/1000)^{0.515} - 1]$.

Standard reference materials were distributed throughout the run to bracket the samples for a total of three analyses of each standard. The average precision for sulfide standards was 0.14% for $\delta^{34}S$ and 0.12% for $\delta^{33}S$ (1 σ , SD). The variance of $\Delta^{33}S$ depends on the precision of the individual measurements of $\delta^{33}S$ and $\delta^{34}S$ where, $\sigma_{\Delta^{33}S}^2 = \sigma_{\delta^{33}S}^2 + \sigma_{\delta^{34}S}^2$. The average precision for $\Delta^{33}S$ was 0.19% (1 σ). Samples with non-zero values ($\Delta^{33}S \neq 0 \pm 0.2\%$) were considered sulfur mass-independent fractionations (S-MIF) and those with near-zero values ($\Delta^{33}S = 0 \pm 0.2\%$) exhibited sulfur mass-dependent fractionation (S-MDF).

The quadruple sulfur isotope composition of representative samples from each lithostratigraphy [BIF (122 m and 115 m), black shale (85.5 m), and metasandstone (50.4 m)] were analyzed by fluorination (SF_6) at the Institut de Physique du Globe de Paris ([Table 2](#)). Approximately ~ 2 mg of Ag_2S were heated in nickel bombs under an excess of F_2 gas (~ 300 torrs) at 350 °C overnight to produce SF_6 gas. The gas was then purified via cryogenic trapping and separation by gas chromatography before introduction to the mass spectrometer (Thermo, MAT 253, run in dual inlet mode). The minor isotopes ^{33}S and ^{36}S are reported in capital delta notation $\Delta^{33}S$, as described above, and $\Delta^{36}S = \delta^{36}S - 1000 \times [(\delta^{34}S/1000 + 1)^{1.89} - 1]$. The $\Delta^{33}S$ and $\Delta^{36}S$ data were reported regarding the Canyon Diablo Troilite (CDT) international standard, with analytical errors of $\pm 0.01\%$ and $\pm 0.2\%$ (2 σ), respectively, based on the reproducibility of analyses of the international standard IAEA S-1. The $\Delta^{33}S$ values determined by fluorination were compared with results from the SO-SO₂ method and $\Delta^{36}S$ values were used to confirm S-MIF or S-MDF relationships.

3.4.4. Total organic carbon and carbon isotopes

Total carbon (TC) concentrations were determined by combustion in an elemental analyzer (Eltra, CHS-580) at 1450 °C in a carrier gas of pure oxygen. Total inorganic carbon (TIC) was measured by acidification in an acidification module (Eltra, TIC Unit). The amount of CO₂ evolved by either combustion or acidification was measured with an infrared cell in the Eltra that was calibrated to standards with known carbon content. Total organic carbon (TOC) is calculated from the difference between TC and TIC, where $TC = TIC + TOC$.

Bulk powdered rocks were analyzed for $\delta^{13}C_{org}$ after carbonate dissolution. Approximately 10 mg of each sample was weighed

Table 2
Estimates of organic matter thermal maturity for RDV.

Estimated peak temperature for OM in RDV (°C)	Reference calibration curve
356.27	Beysac et al. (2002)
353.86	Rantitsch et al. (2004)
282.62 \pm 50	Rahl et al. (2005)
411.73 \pm 30	Aoya et al. (2010)

into a silver cup (5 mm × 9 mm) and wetted with 50 µL of ultra-pure water (Milli-Q, 18 MΩ). The unsealed cup was set in a heat resistant 96-well plate placed in a glass desiccator containing a beaker of fuming 12 N HCl to destroy the carbonates. The samples were decarbonated in the sealed desiccator for 6 to 8 h. After acidification, the samples were dried at 50 °C on a hot plate for 24 h. The dried silver cups were then wrapped in tin cups (5 mm × 9 mm) before carbon isotopic analysis. The samples were combusted to carbon dioxide gas in an elemental analyzer (Thermo, EAIsolink) coupled under continuous flow to a stable isotope ratio mass spectrometer (Thermo, DeltaV Plus) in the Stable Isotope Biogeochemistry Laboratory at Indiana University-Purdue University Indianapolis. Carbon isotope values were reported relative to Vienna Pee Dee Belemnite (VPDB) by normalization to three reference materials (Buffalo River Sediment = −19.86‰; USGS-40 = −26.39‰; IAEA CH6 = −10.45‰). All isotopic values were calculated according to standard notation in per mil (‰) according to: $\delta^{13}\text{C} = [((^{13}\text{C}/^{12}\text{C})_{\text{sample}})/((^{13}\text{C}/^{12}\text{C})_{\text{VPDB}}) - 1] \times 10^3$. Analytical precision of standards ($n = 7$) was less than $\pm 0.2\text{‰}$.

4. Results

4.1. Petrography

4.1.1. Banded iron formation

The BIF is composed of regular millimeter alternating bands of light quartz-carbonate (chert facies) and dark carbonate-pyrite

(sulfide facies) associated with films of organic matter (Fig. 4A and B). Accessory minerals such as sericite, actinolite, and rutile are present. Pyrite is the major authigenic sulfide mineral and chalcopyrite and arsenopyrite were rarely observed. The bedding (S_0) of BIF deposition is preserved in hand sample and as alternate layers of quartz and carbonate. A superimposed schistosity (S_1) is indicated by stretched quartz and the preferential orientation of carbonate and pyrite parallel to the foliation plane. A crenulation cleavage (S_2) is locally present, marked by a few oxides and pyrites and associated pressure shadows rotated along the crenulation plane. A metamorphic event is recorded by coarser-grained carbonate and quartz overgrowth or recrystallization associated with actinolite and sericite but hydrothermal minerals such as albite or muscovite were not observed.

Two generations of disseminated pyrites were observed, one mainly diagenetic and one epigenetic that occurs more rarely. The epigenetic pyrites (<50 µm) are euhedral to subhedral and associated with foliated or crenulated actinolite, sericite, and recrystallized quartz consistent with a metamorphic origin. Diagenetic pyrites (euhedral and subhedral grains) are smaller in general (from < 20 µm to < 50 µm) and well preserved, with cubic edges in contact with the chemical sedimentary protolith of quartz and carbonate, not replacing any minerals (Fig. 4C–F).

4.1.2. Black shale

The black shale is composed of organic matter associated with clay- and silt-size sericite, carbonate, and quartz (Fig. 5A). Acces-

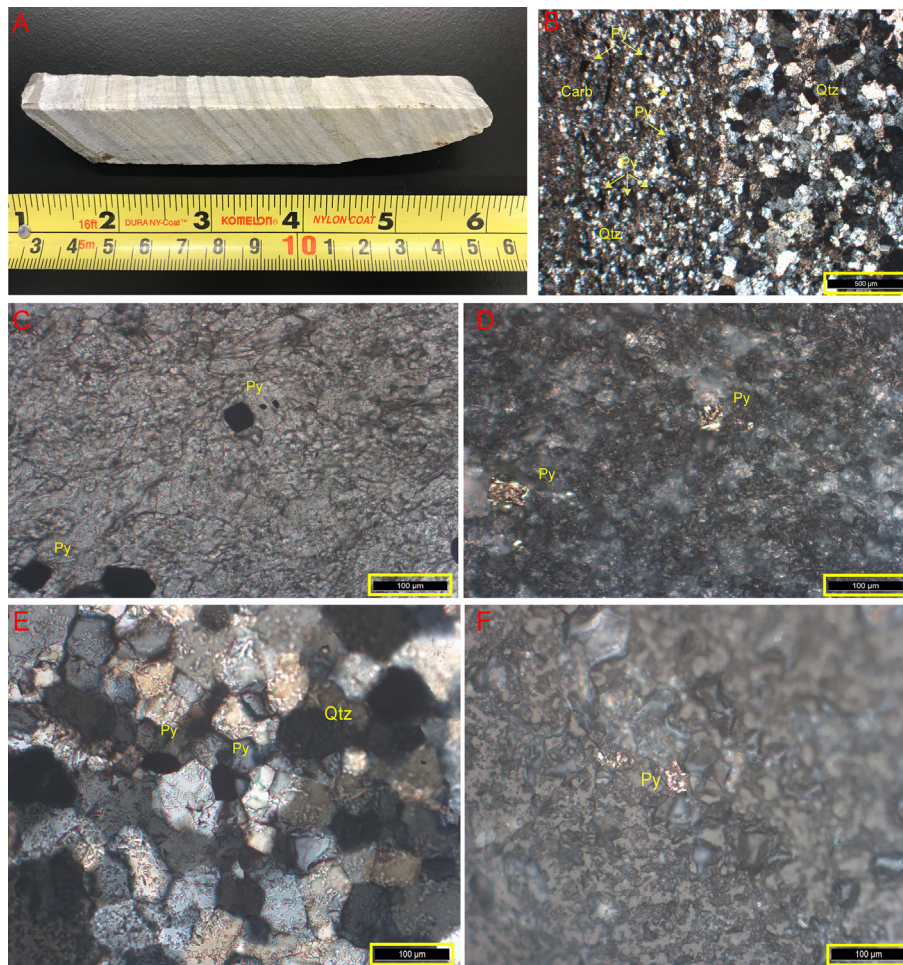


Fig. 4. (A) BIF hand sample; (B) Contact between bands at 119 m depth, quartz and carbonate (protolith) and a portion of recrystallized quartz, and disseminated pyrite grains (<50 µm); (C) and (D) Euhedral pyrites (<20 µm and < 50 µm) associated with primary carbonate; (E) and (F) Subhedral pyrite grains (<50 µm) associated with protolith quartz; C is in transmitted light; B and E are in transmitted light crossed nicols, and D and F are in reflected light; pyrite (Py); quartz (Qtz); carbonate (Carb).

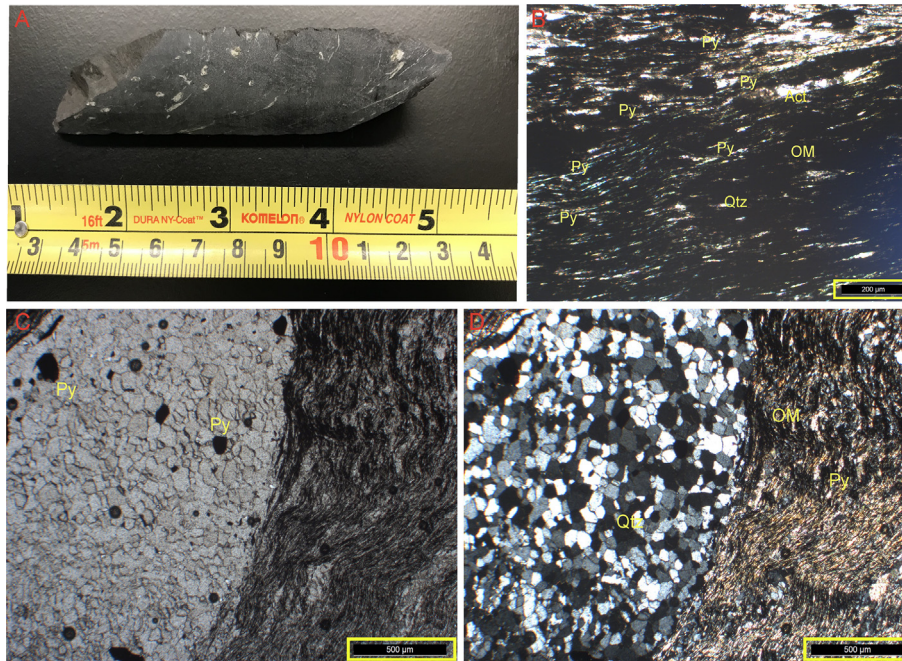


Fig. 5. (A) Black shale hand sample thin sections; (B) Organic matter fringes with disseminated pyrite grains, generally small (<20 μm) at 82 m depth; (C) and (D) Contact between recrystallized quartz and organic matter fringes at 91.3 m depth. Euhedral to subhedral pyrite grains found disseminated in <100 μm in the quartz and <50 μm in the organic matter. C is in Transmitted light; B and D are in transmitted light crossed nicols; organic matter (OM); pyrite (Py); quartz (Qtz); carbonate (Carb); actinolite (Act).

sory minerals include pyrite, chlorite, actinolite, and Fe and Ti oxides. The shale consists of mostly continuous, wavy, and straight parallel laminae, defining the detrital sedimentary protolith bedding (S_0). Very fine to fine-grained sand-size particles rich in quartz and carbonate form bands that are up to 1000 μm thick. Organic matter occurs throughout the thin section as a black material with low crystallinity and considerable structural disorder. The higher organic matter content appears to correlate with the more pronounced development of laminations and clay-silt-granulometry (Fig. 5B). Inputs of sand-sized particles, reduction in organic matter content, and graded bedding could suggest marine regression cycles. Occasionally, stretched quartz, carbonate, and sericite form schistosity planes (S_0/S_1), and dynamic recrystallization can develop strain fringes of quartz and crenulation cleavage (S_2 microfolds).

Diagenetic pyrite occurs as disseminated subhedral crystals (<20 μm , Fig. 5C and D) associated with organic matter. Subhedral and anhedral (from <20 to <100 μm) detrital varieties (<2%) occur in the quartz and carbonate protolith matrix (Fig. 5C and D). Some detrital grains have been rotated, developing quartz strain fringes. No other sulfides were observed.

4.1.3. Metasandstone

The finely laminated and thinly bedded metasandstone consists essentially of carbonate and quartz, with minor amounts of actinolite, chlorite, pyrite, and trace occurrences of sericite, plagioclase, Fe, and Ti oxides (Fig. 6). Carbonates, calcite or ankerite, are fine-grained and strongly intermingled with quartz. Phyllosilicate minerals and flattened quartz crystals define a weak foliation (S_1) parallel to the sedimentary bedding (S_0), and localized boudinage and crenulation cleavage can be seen. The quartz vein occurs in this unit, and no more than 5 cm of continuous quartz was observed (Fig. 6E) in association with albite and muscovite. Potential alteration by hydrothermal circulation is highly localized and near the quartz vein, represented by silicification and albitization as veinlets replacing other feldspars and mafic silicates (discussed

in more detail in Section 5.1). Sulfides are mostly pyrite, whereas chalcocopyrite and arsenopyrite were rarely observed in thin-section.

Similar to the BIF petrography, two generations of pyrite were identified: diagenetic and epigenetic. Coarser-grained epigenetic pyrite (~300–800 μm) associated with actinolite and chlorite is aligned parallel to the schistosity and crenulation cleavage planes (elongated, anhedral Fig. 6F and G). Larger epigenetic pyrite (up to 0.5 cm) shows evidence that earlier crystals of diagenetic pyrite acted as sites of nucleation and overgrowth. This late growth metamorphic pyrite was rotated, associated with recrystallized quartz forming strain fringes. Diagenetic pyrite euhedral (cubic) to subhedral, undeformed (~200–20 μm), occur around and between detrital grains of quartz and carbonate (Fig. 6). Some of the subhedral-euhedral pyrites were resorbed into anhedral pyrite rims and overgrowths.

4.2. Age constraint

A total of 55 detrital zircon grains were analyzed for U-Pb isotopes, and all spots are plotted in the concordia diagram (Fig. 7A). The sample shows little Pb loss towards zero and most of the grains cluster in the range between ca. 3.27 Ga and 2.76 Ga, with a few older grains. From the 55 analyzed zircon grains, 44 within 10% discordance were used in the probability density plot (Fig. 7B; Table S3). For these grains, the oldest single zircon $^{207}\text{Pb}/^{206}\text{Pb}$ age is 3514 ± 14 Ma, whereas the youngest single zircon is 2760 ± 19 Ma. The weighted average of the three younger zircon grains was used to calculate the maximum depositional age of 2763 ± 11 Ma (MSWD = 0.097). The majority of grains are from two age populations. The youngest population was estimated at 2787 ± 11 Ma ($n = 11$), whereas the oldest population was calculated at 3251 ± 12 Ma ($n = 10$).

4.3. Thermal constraints on organic matter

A polished thin section of black shale from 82 m depth (Fig. 8A) in the RDV core was analyzed by micro-Raman spectroscopy.

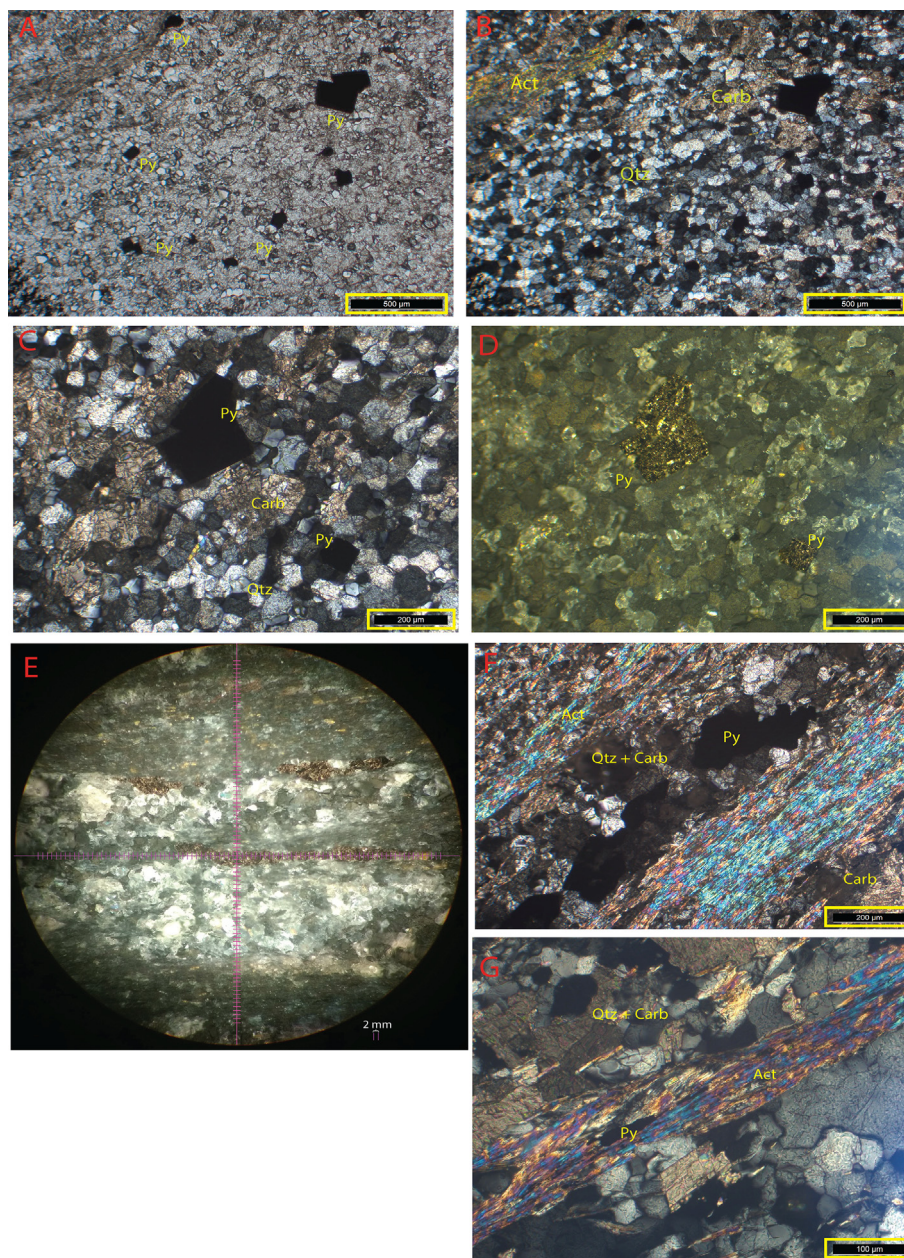


Fig. 6. Metasandstone thin sections. Euhedral to subhedral pyrites (grains from $<200\ \mu\text{m}$ to $<40\ \mu\text{m}$) associated with sedimentary protolith represented by quartz and carbonate at 63 m (A and B) and 70.4 m (C and D) depth. Mineralized quartz vein between 68.3 and 69.3 m (E). Elongated, anhedral pyrite in paragenesis with quartz (F) and actinolite (G), aligned parallel to the schistosity. A is in transmitted light, B, C, E, F and G are in transmitted light crossed nicols and D is in reflected light; pyrite (Py); quartz (Qtz); carbonate (Carb); actinolite (Act).

Width, location, and area values of D1, D2, and G bands were identified in the spectra (Fig. 8B). The calculated values for R1 and R2 were 0.8419 and 0.6258, respectively. The peak temperature reached by the organic matter associated with regional metamorphism or hydrothermal alteration, calculated with the four different calibration curves, indicates a temperature range between $282.62\ ^\circ\text{C}$ and $411.73\ ^\circ\text{C}$ (Table 2).

4.4. Geochemistry

The bulk rock concentrations of major and trace elements are shown in Supplementary Data (Table S1). Major elements Al and Fe_T varied from 1.4 to 12.3 wt.% and from 1.1 to 26 wt.%, respectively, with a tendency to decrease up-core between the lithotypes (Supplementary Data, Table S1). Elements with relatively low geo-

chemical mobility include REE, Hf, Zr, and Y. The sum of REE varied between 8.4 and $186\ \text{mg kg}^{-1}$ (or 1 and $15\ \text{mg kg}^{-1}$, when normalized to Post-Archean Australian Shale; PAAS), with the higher concentrations in the black shale relative to units above and below. Variations through RDV of light rare earth elements (LREE) are relatively higher (e.g., La in average $16.5 \pm 7.4\ \text{mg kg}^{-1}$) compared to HREE (e.g., Lu in average $0.19 \pm 0.06\ \text{mg kg}^{-1}$). Yttrium varied from 3.7 to $16.5\ \text{mg kg}^{-1}$ and Hf from 0.3 to $5.5\ \text{mg kg}^{-1}$, both reaching maximum values within the black shale. Variations in Zr ($96 \pm 34\ \text{mg kg}^{-1}$) followed the same behavior with lower concentrations in the top and bottom lithologies. In addition to REE, Zr and Hf other high-field-strength elements, Nb ($3.6 \pm 1.7\ \text{mg kg}^{-1}$), U ($1.6 \pm 0.9\ \text{mg kg}^{-1}$), and Th ($5.1 \pm 2.9\ \text{mg kg}^{-1}$) also had higher concentrations within the black shale, although with lower variability between lithologies (Supplementary Data, Table S1). Highly

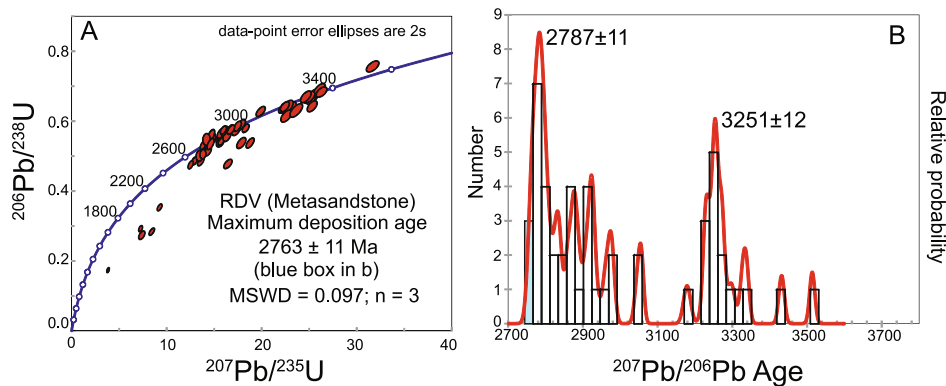


Fig. 7. U-Pb LA-ICP-MS results for detrital zircon grains of the metasandstone sample of the RDV drill core. (A) Concordia diagram plotting all of the analyzed zircon grains and maximum depositional age of 2763 ± 11 Ma. (B) Probability density plot of zircon grains that are less than 10% discordant, highlighting two main age peaks.

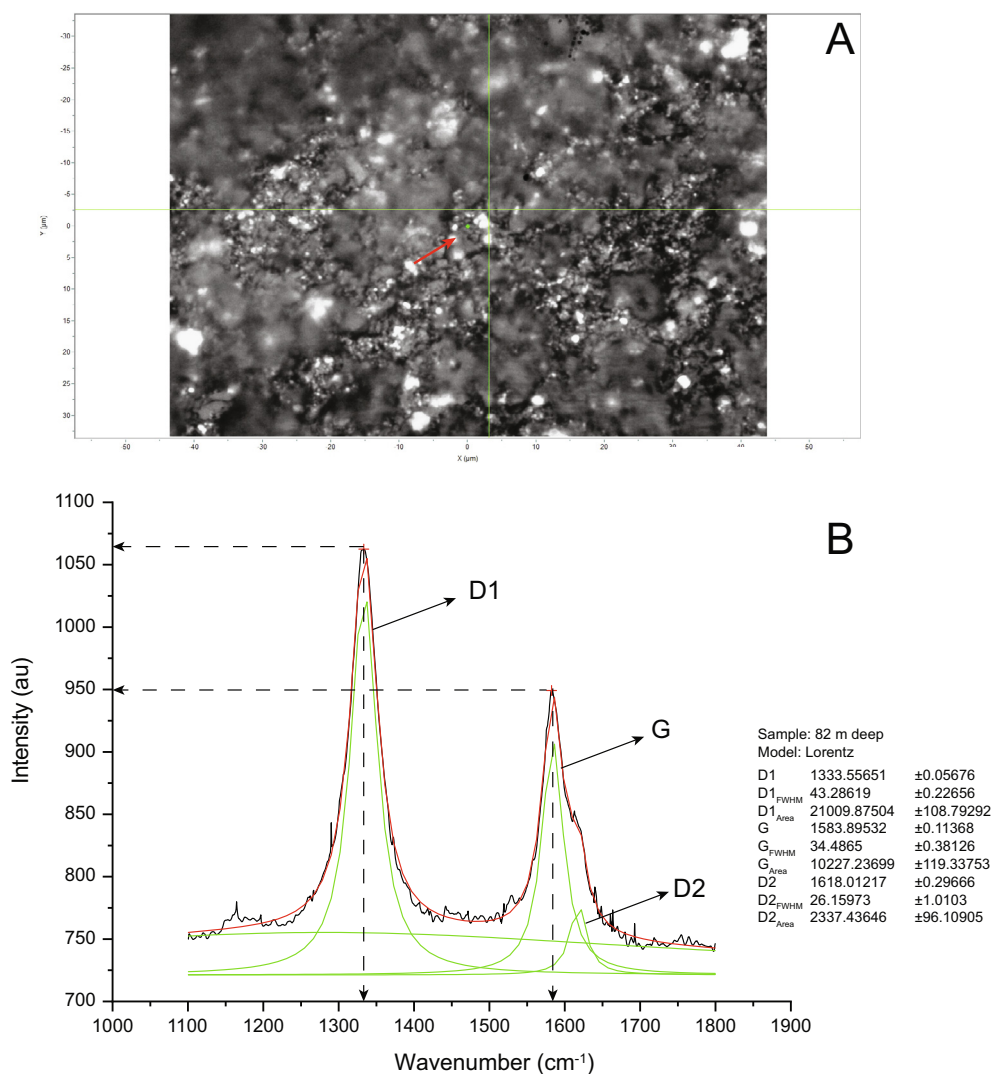


Fig. 8. First-order Raman bands of organic matter spectra of black shale sample at 82 m depth. (A) Organic matter in Raman imaging spectroscopy with 100× magnification. (B) Full-width half maximum (FWHM) area (Area) and peak positions D1, G, and D2.

mobile elements associated with potassic and sodic alterations, Sr ($5.2\text{--}232$ mg kg⁻¹), Ba ($0.4\text{--}470$ mg kg⁻¹), and Rb ($0.2\text{--}175$ mg kg⁻¹), were highly variable with lower levels observed within the BIF when compared to the black shale and metasandstone.

Elements associated with mafic rocks, Cr ($4.4\text{--}629$ mg kg⁻¹), Ni ($13\text{--}307$ mg kg⁻¹), and Zn ($20\text{--}617$ mg kg⁻¹), have higher yet variable concentrations in the BIF relative to the more uniform concentrations in the lithologies above. Bismuth ($0.02\text{--}0.58$ mg kg⁻¹)

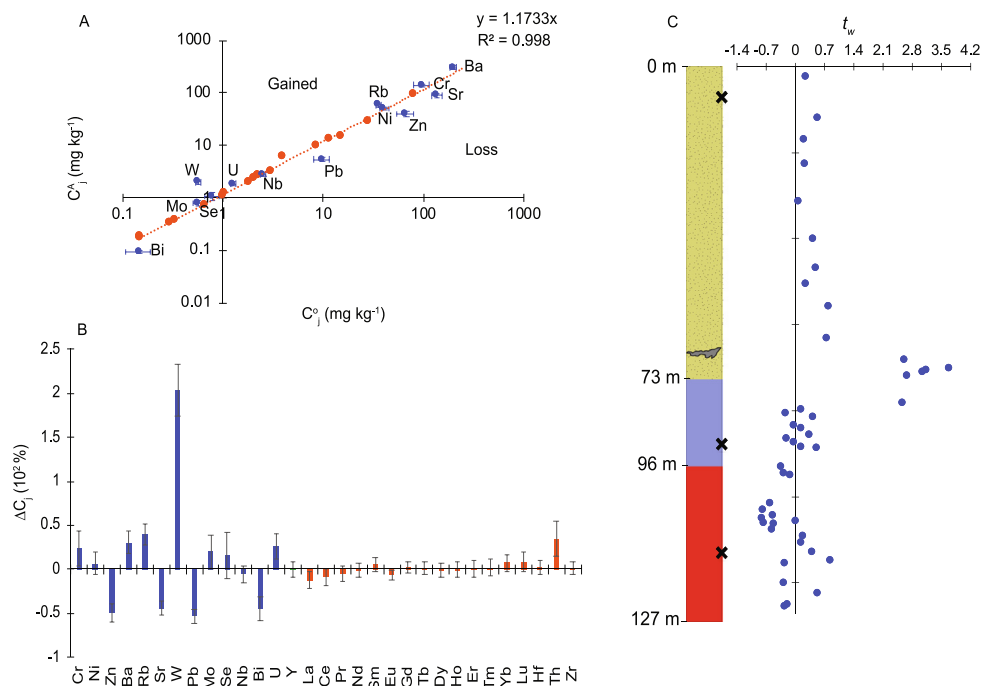


Fig. 9. Assessing element mobility associated with potential hydrothermal alteration. (A) Mass change for W (t_w , considering the reference sample as the one where concentrations are closer to the lithology average) through RDV. (B) The Isocon (Grant, 1986) best-fit for average concentrations of immobile elements (Hf, Zr, REE, Th, Y; in orange) in samples from 73 to 68 m depth (near the quartz vein, gray horizontal lense) and from 63 to 0 m (away from the quartz vein). Concentrations of mobile elements representing relative gain or loss are in blue. (C) Change in the concentration of a component (ΔC_i) proximal to the quartz vein (73–68 m) relative to its concentration in less altered samples (63–0 m).

concentrations were also higher within the BIF, although samples in the proximity of the quartz vein exhibited a clear trend of enrichment (Supplementary Data, Table S1). Metals potentially associated with hydrothermal gold mineralization such as Mo ($0.32\text{--}5.3\text{ mg kg}^{-1}$) and Se ($0.26\text{--}3.39\text{ mg kg}^{-1}$) were broadly similar throughout the core, compared to the much greater variability in concentrations of Pb ($3\text{--}43\text{ mg kg}^{-1}$) and W ($0.4\text{--}22\text{ mg kg}^{-1}$), that reached peak concentrations within the lower metasandstone.

Gain or loss of trace elements associated with potential hydrothermal alteration is shown in Fig. 9A. Relative to the upper metasandstone (63 to 0 m depth), samples closer to the quartz vein (68–73 m) exhibited gains in Cr ($24\% \pm 20\%$), Ni ($6\% \pm 12\%$), Ba ($30\% \pm 13\%$), Rb ($40\% \pm 12\%$), W ($204\% \pm 29\%$), U ($26\% \pm 14\%$) and Th ($35\% \pm 19\%$, Fig. 9B). Loss of Zn ($50\% \pm 10\%$), Sr ($44\% \pm 8\%$), Pb ($53\% \pm 8\%$) and Bi ($45\% \pm 13\%$) was also observed (Fig. 9B). Considering $\pm 70\%$ as the threshold for anomalous gain or loss of element mass (Lebrun et al., 2017), W is the only element with significant gains (Fig. 9B). The W anomaly that exhibits a mass gain of up to 370%, is localized to the quartz vein (69 m depth; Fig. 9C).

Iron speciation ratios ($\text{Fe}_{\text{HR}}/\text{Fe}_{\text{T}}$ and $\text{Fe}_{\text{Py}}/\text{Fe}_{\text{HR}}$) and mineral phases (Fe_{Py} , Fe_{Carb} , Fe_{Oxi} , Fe_{Mag}) are shown in Supplementary Data (Table S2) and Fig. 10. Highly reactive iron (Fe_{HR}) ranged from 8 to 100 wt.% of the bulk iron and systematically decreased up-core. Fe_{HR} contributions were higher, on average, $52 \pm 26.5\text{ wt.}\%$ with variable $\text{Fe}_{\text{HR}}/\text{Fe}_{\text{T}}$ that was greater than 0.2, within the BIF and the black shale (Supplementary Data, Table S2). These values are lower in the metasandstone, Fe_{HR} was less than 38 wt.%, and $\text{Fe}_{\text{HR}}/\text{Fe}_{\text{T}}$ was below 0.38. In the BIF, the contribution of Fe_{Carb} to the Fe_{HR} pool exceeded all the other mineral phases (from 31 to 91 wt.%) and was higher than in the other rock units (Supplementary Data, Table S2 or Fig. 10). In the black shale, the contribution of Fe_{Py} and Fe_{Carb} were similar and highly variable (between 7 and 87 wt.% of the Fe_{HR} pool), while in the metasandstone, Fe_{Mag} and Fe_{Oxi} exceeded 10 wt.% of the Fe_{HR} pool (Supplementary Data, Table S2).

The sulfur isotopic composition of chromium reducible sulfides ($\delta^{34}\text{S}$ and $\Delta^{33}\text{S}$, Supplementary Data, Table S2) was variable throughout the core, with $\delta^{34}\text{S}$ ranging from -3.1‰ to 6.9‰ and $\Delta^{33}\text{S}$ from -0.69‰ to 3.4‰ (Fig. 10). Overall, $\delta^{34}\text{S}$ increased to $\sim 4\text{‰}$, and $\Delta^{33}\text{S}$ values decreased to $\sim 0\text{‰}$ up the core. Most sulfides in the lower lithologies (BIF and black shale) were consistent with S-MIF ($\Delta^{33}\text{S} \neq 0 \pm 0.2\text{‰}$), while those in the upper lithostratigraphy (metasandstone) were not consistent with S-MIF or were very close to the S-MDF threshold (see Section 5.4 for discussion).

TOC concentrations ($0.68\text{--}7.8\%$; Supplementary Data, Table S2) were higher ($4.58\% \pm 1.8\%$) in the black shale relative to units below and above. $\delta^{13}\text{C}_{\text{org}}$ varied from -44‰ to -17.5‰ (Supplementary Data, Table S1) throughout RDV and was positively correlated ($R^2 = 0.56$, $p < 0.001$) with TOC content (Fig. 10). $\delta^{13}\text{C}_{\text{org}}$ values were lowest in the BIF ($-32.7\text{‰} \pm 7\text{‰}$). Despite large variations throughout the core, $\delta^{13}\text{C}_{\text{org}}$ values in the top 50 m were relatively uniform ($-34.5\text{‰} \pm 1.6\text{‰}$).

5. Discussion

5.1. Assessment of post-depositional alteration

It has long been understated in the study of Archean biogeochemistry that the majority of the rock record was submitted to post-depositional alterations (Planavsky et al., 2020). The potential for chemical overprints by modern weathering, metamorphism, or hydrothermal alteration (Muller et al., 2017; Kresse et al., 2018; Slotznick et al., 2018; Stüeken et al., 2019; Wang et al., 2019) were evaluated before interpreting the chemostratigraphy of RDV. Modern oxidative weathering of the RDV subsurface drill core is highly unlikely as the core was obtained in an underground mine. Element mobility associated with hydrothermal systems can lead to gains or loss of material, rendering equivocal interpretations of primary or diagenetic geochemistry. The potential for secondary

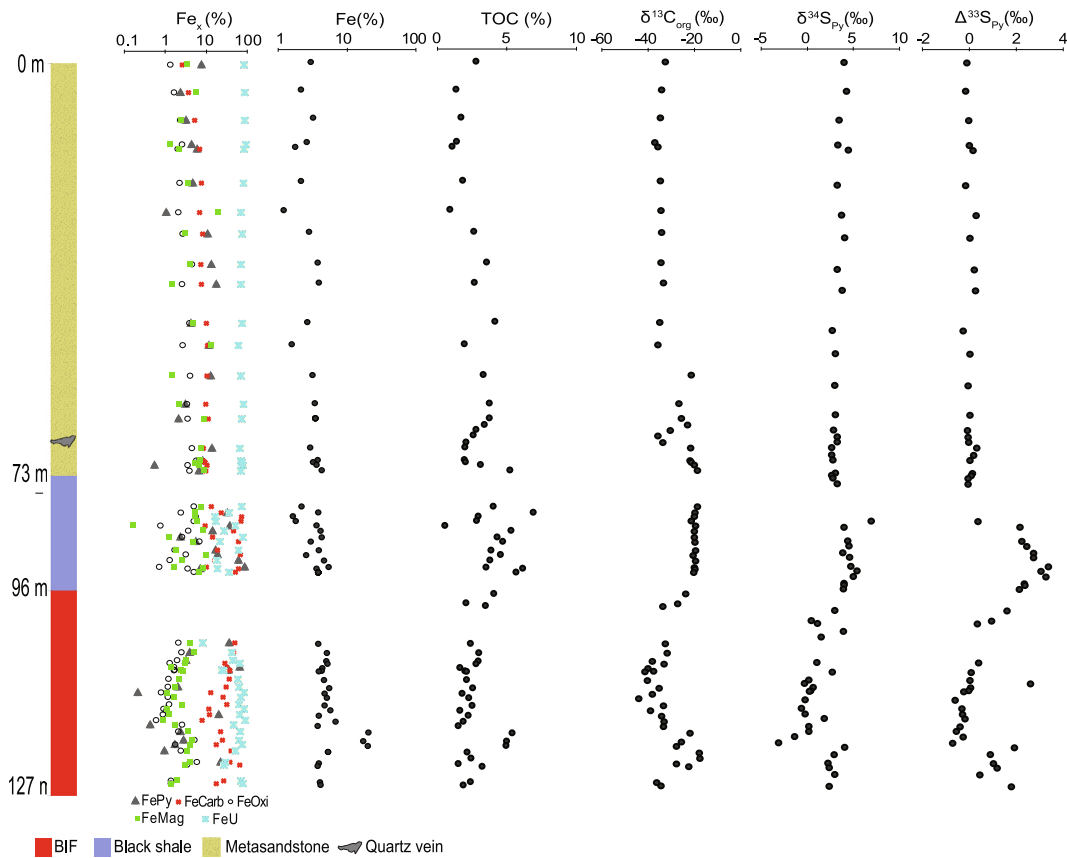


Fig. 10. Chemostratigraphy of the RDV core, including iron speciation phases, sulfur isotopes ($\delta^{34}\text{S}$ and $\Delta^{33}\text{S}$), organic carbon content (TOC %), and isotopic composition ($\delta^{13}\text{C}_{\text{org}}$).

alteration of the primary signatures can be evaluated with a combined approach of petrography and geochemistry (Planavsky et al., 2020). Assessing the gold mineralization footprint is, therefore, necessary in this study to establish reliable paleoenvironmental interpretations.

The compositional layering of quartz and carbonate (the sedimentary protolith) is parallel to unit boundaries and therefore considered to be parallel to original bedding (S_0). However, petrographic observations indicate that the mineral assemblage of actinolite and chlorite is typical of greenschist facies metamorphism of graywacke and psammite (Bucher and Grapes, 2011). The potential for post-depositional hydrothermal fluids alteration was investigated throughout all lithologies. Hydrothermal minerals were not observed in the petrographic thin section located just above the quartz vein (Fig. 6A and B), suggesting that the fluid circulation is highly localized and proximal to the quartz vein. Pervasive albitization, silicification and the presence of fine-grained muscovite is suggestive of the passage of a potassic and silica-rich fluid. This fluid, however, is restricted to the mineralization alteration halo (as defined below).

Hydrothermal gold input in the Roça Grande deposit is estimated between 1% and 5% (Araújo and Lobato, 2019). Overall, mineralized gold is associated with quartz veins that occur locally in the vicinity of associated sulfides (Araújo and Lobato, 2019). Nova Lima Group metasediments that host gold have narrow alteration haloes (e.g., Cuiabá deposit, Lobato et al., 1998; Araújo and Lobato, 2019). Although chemical changes linked to sulfidation commonly involve the addition of S and Au and the removal of organic carbon (Lobato et al., 1998; Ribeiro et al., 2015; Kresse et al., 2018), the chemostratigraphy of RDV suggests the quartz

vein does not represent a significant hydrothermal mineralization input from the deposit. Fe_{py} in the vicinity of the vein is similar to concentrations throughout the metasandstone (Supplementary Data, Table S2; Fig. 10) and therefore inconsistent with an anomalous addition of hydrothermal pyrite. The TOC exhibits a localized decrease at the depth of the quartz vein (Supplementary Data, Table S2; Fig. 10); however, this excursion appears restricted to the lower metasandstone.

Mass balance calculations (Eq. 1) were used to characterize the extent of elemental enrichment or depletion within proximity of the quartz vein. Overall, geochemical changes related to mineralization are observed towards the quartz vein both up and down-core (Fig. 9). The Isocon normalization approach (Fig. 9A and B) demonstrates gain and loss of mobile elements in metasandstone samples proximal to the quartz vein (between 68 and 73 m depth). Samples above this zone (63 to 0 m depth) exhibit neither gain nor loss in element distribution. Geochemical correlations between elements also exhibit a unique distribution in samples proximal to the ore zone (Supplementary Data, Fig. S1). Strong positive correlations, such as between Ni and TOC (around +1) or negative correlations between W and Zn (around -1), are only observed near the quartz vein (Supplementary Data, Fig. S1). Analyte relationships in the upper metasandstone, black shale, or BIF are generally muted relative to those near the quartz vein. This comparative framework demonstrates that alteration is constrained to the lower metasandstone.

Metal associations in gold mineralization zones (Lobato et al., 1998; Oliver et al., 2015; Lebrun et al., 2017; Tedeschi et al., 2018) provide another approach to assess alteration potential. In the Rio das Velhas Greenstone Belt, enrichments in Au-Ag-As-Sb-

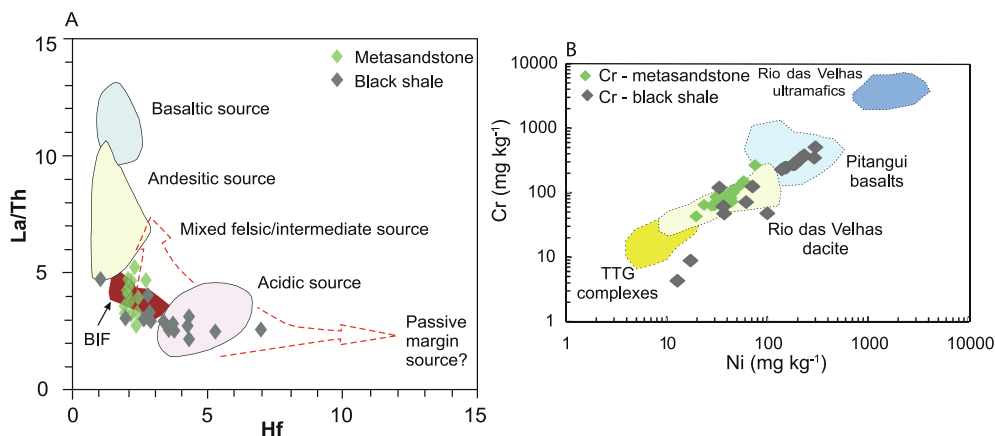


Fig. 11. Potential sources for metasedimentary rocks of the Rio das Velhas Greenstone Belt in the Roça Grande gold deposit (modified from Floyd and Leveridge, 1987). BIF samples plot in the field as indicated by the arrow. Cross plots of trace element distributions (A) La-Th-Hf and (B) Cr-Ni indicate mixed felsic-intermediate sedimentary sources to RDV. Mafic and ultramafic rock data are from Verma et al. (2017), dacite from da Silva et al. (2017), basement TTG complexes from Farina et al. (2015).

W are a common feature of gold mineralization (e.g., Ribeiro-Rodrigues et al., 2007; Araújo and Lobato, 2019).

Fluids relatively enriched in W were described for the Lamego deposit stratigraphically below the Roça Grande in the Morro Vermelho Formation (Araújo and Lobato, 2019). A significant gain in W mass (>70%; see 3.4.1 for description) is observed close to the quartz vein (Fig. 9B and C) in RDV. Away from this zone, the amount of W is no different than background levels found in other lithologies (Fig. 9C). When placed in context, the W enrichment in RDV is modest compared to those observed in hydrothermal zones associated with gold deposits (e.g., Lebrun et al., 2017; Tedeschi et al., 2018) that can reach values as high as 16,361% and cooccur with silicification (Zhang et al., 2018). In addition to W, other elements associated with gold mineralization (Mo, Se, and Ba; Hood et al., 2019) also exhibited modest mass gains (when calculated with Eq. 2) within the samples from 73 to 68 m depth. Bismuth is another index element associated with gold mineralization (e.g., Oliver et al., 2015; Hood et al., 2019). However, in RDV, the quartz vein showed a mass loss in Bi related to the less altered metasandstone samples.

In the proximity of the quartz vein, the enrichment of Ba and Rb could also be associated with potassic alteration (Hood et al., 2019), while discrete gains in Ni and Cr are probably related to hydrothermal fluid percolation from the underlying mafic rocks from the Rio das Velhas Supergroup. Zinc is associated with gold in many deposits, including in the Rio das Velhas Supergroup. However, within RDV, the altered zone was depleted in Zn, which might be related to chemical oxidation. Low mobility or immobility was observed for Nb, Hf, Zr, and REE, including the altered zone.

Based on trace element mass balance, we propose that the alteration is highly localized and limited to within 17 m of the quartz vein, between ~80 and 63 m depth (Fig. 9). Therefore, we argue that the RDV drill core is suitable for biogeochemistry interpretations if samples from 80 to 63 m depth are considered with caution in the discussion of iron speciation, C and S isotope systematics. The possible role of fluid processes and temperature on each proxy are discussed in the relevant sections below.

5.2. Stratigraphic position, age constraints, and sediment source

Banded iron formations are a common feature of the Morro Vermelho Formation, typically observed in the basal member of the “undivided Morro Vermelho” (Araújo et al., 2020a). These BIFs, such as the one in RDV, have mm to cm-thick layering and are in contact with both metavolcanic and clastic metasedimentary rocks

as well as layers of carbonaceous phyllite (Araújo et al., 2020a). The maximum depositional age of RDV (2763 ± 11 Ma) within the Morro Vermelho Formation is consistent with the youngest maximum depositional age of the overlying Mestre Caetano Formation at 2773 ± 7 Ma (Noce et al., 2005; Araújo et al., 2020b) and the maximum depositional age of the Maquiné Group at 2730 Ma (Moreira et al., 2016). Moreira et al. (2016) also found a progressive decrease of younger ages towards the top of the Maquiné Group, which overlies Nova Lima Group, with the bottom sequence maximum deposition age at ca. 2745 Ma, the middle sequence at 2735 Ma, and the top sequence at 2718 Ma, that suggest sediment accumulation during an evolving volcanic event. This *syn*-orogenic event requires that sedimentation was concomitant with exhumation of a proximal arc, with maximum deposition ages very close to the timing of deposition and representative of volcanic events.

For the purposes of the present study the most crucial age constraint is related to the Rio das Velhas Supergroup minimum age. Moreira et al. (2019) constrained the age of the Supergroup using felsic intrusions (samples A1 and A2 from Moreira et al., 2019) within schists that yield crystallization ages of 2948 ± 3 Ma and record high-grade metamorphism at 2700–2690 Ma. This high-grade zircon was suggested to be found in-situ, and therefore, constrains the minimum age of the sequence at 2690 Ma (Moreira et al., 2019).

Trace element plots of the RDV metasedimentary rocks indicate provenance from mixed felsic-intermediate sources with a minor contribution from basaltic, felsic, and recycled sources (Fig. 11). Dacite from the Rio das Velhas Greenstone Belt (2772 ± 6 Ma eruptive event at the Greenstone Belt, da Silva et al., 2017) and tonalite from the TTG gneiss domes are intermediate rocks and potential clastic sources for the metasedimentary rocks. Based on geochemistry and geochronology data, we suggest dacite as the main source for the original sediments in RDV and therefore, sediment accumulation occurred concomitantly with volcanic events, placing it in the Neoproterozoic, approximately 300 Ma before the GOE.

5.3. Iron speciation and redox implications

Iron minerals have different reactivities to dissolved sulfide, and the relative distribution of reactive iron within the rock can provide constraints on redox conditions during deposition and early diagenesis (Raiswell and Canfield, 1998; Poulton and Raiswell, 2002; Poulton and Canfield, 2011). However, the mobility of iron during fluid percolation and the potential for iron exchange among different reservoirs (Fe_{Py} , Fe_{Carb} , Fe_{Oxi} , Fe_{Mag} , Fe_U) at elevated tem-

perature and pressure complicate paleo-redox interpretations (Reinhard et al., 2013; Slotznick et al., 2018). Although metamorphism and hydrothermal alteration challenge the use of the traditional reactive iron ratios (Fe_{HR}/Fe_T and Fe_{Py}/Fe_T), petrography combined with a knowledge of the sedimentary protolith and the relative distribution of iron minerals can help to interpret redox changes and secondary processes.

The proportion of Fe(III) minerals, Fe_{Oxi} (<4%), and Fe_{Mag} (<5%) remains relatively low throughout the RDV, except for a few samples within the black shales. In contrast, Fe(II) minerals, Fe_{Py} and Fe_{Carb} , are the fractions of the iron pool that drive significant variations in Fe_{HR}/Fe_T . Overall, the chemically extracted iron from 127 to 78 m depth in the BIF and part of black shale lithology agrees with the petrography, which shows a predominance of Fe_{Carb} , a relatively high contribution of Fe_{Py} (which with Fe_{Carb} accounts for 97% of Fe_T), and the remainder Fe_U (mostly silicates). The predominance of Fe(II) in the lower core (>78 m depth) and high Fe_{HR}/Fe_T (on average 0.8 ± 0.6) in the black shales indicates reducing conditions that may reflect depositional or post-depositional geochemistry. At 78 m depth, a sharp decrease in Fe_{HR} is observed, and much lower Fe_{HR}/Fe_T values (<0.38) could indicate oxidizing conditions.

The mobilization of diagenetic iron from carbonates into silicate minerals during post-depositional temperature increase has been described before (Slotznick et al., 2018) and could account for the sharp decrease in Fe_{HR} observed at 78 m depth. Otherwise, a decreased contribution in reduced iron phases (Fe_{Py} and Fe_{Carb} , Fig. 10) could be a consequence of hydrothermal fluid infiltration associated with the quartz vein formation. However, as mineralization is associated with sulfidation (see section 5.1), Fe_{Py} would otherwise be expected to increase. It is also important to note that the sharp decrease in Fe_{HR} is accompanied by a smooth decline in Fe_T up-core (maximum of 26% in the BIF, 6% in black shale, and 4.4% in the metasandstone). Such an observation could indicate that Fe is more sensitive to hydrothermal processes than other trace elements, a change in the water column chemistry, or most likely, an influence of lithology, with a higher contribution of siliclastic particles.

Another potential effect described for hydrothermal alteration in the distribution of iron minerals is the mobilization of primary Fe_{Py} (authigenic or early diagenetic) to secondary sulfides (such as pyrrhotite) (Ferry, 1981; Slotznick et al., 2018). However, pyrrhotite was not observed in any representative thin sections investigated (Figs. 4–6). On the other hand, if pyrrhotite were present in samples not analyzed for petrography, the mineral would be potentially double-counted in more than one of the Fe_{Py} , Fe_{Carb} , Fe_{Oxi} , Fe_{Mag} phases because iron from pyrrhotite can be extracted in any or all acidification steps of the sequential iron procedure (Reinhard et al., 2013; Slotznick et al., 2018). The low pH conditions of chromium reduction (pH = 1), sodium acetate and buffered dithionite (pH = 4.8), or oxalate (pH = 3.2) extractions can totally or partially dissolve pyrrhotite (Chang and Kirschvink, 1985; Prahara and Fortin, 2004; Reuschel et al., 2012; Schumann et al., 2012; Partin et al., 2015) and result in the inclusion of pyrrhotite iron into the incorrect or multiple Fe_{HR} pools. A misassignment of iron pools would suggest a more significant amount of Fe_{HR} and mask the relative Fe_U contribution to Fe_T . However, Fe_{HR} is a feature of anoxic water columns, and therefore the presence of pyrrhotite makes the paleo-redox interpretations on Fe_U contribution conservative.

5.4. The biological rise of oxygen and S-MIF preservation

Carbon and sulfur isotopes are discussed together to evaluate the connection between their biogeochemical cycles in the Neoproterozoic (Zerkle et al., 2012; Thomazo et al., 2013; Izon et al., 2015; Williford et al., 2016). $\delta^{13}C_{org}$, $\delta^{34}S$, and $\Delta^{33}S$ exhibit

coincident geochemical behavior towards higher values through the lithologic change from BIF to black shale and decrease to lower values within the black shales at 79 m depth (Fig. 10).

The wide range of $\delta^{13}C_{org}$ values between -44‰ and -17.5‰ (Fig. 10) observed in the BIF suggest a diverse spectrum of carbon fixation pathways with biomass from heterotrophs such as methanotrophs or sulfate reducers. Biological activity operating as a potential oxidative mechanism that transforms dissolved hydrothermally-derived Fe(II) into solid-phase Fe(III) has many implications for iron formation deposition during the Precambrian. The BIF-carbonate is the most debated facies (Bekker et al., 2010; Johnson et al., 2013; Köhler et al., 2013) since there is considerable speculation about its origin, including: co-precipitation of Fe(II) with bicarbonate in the water column; mediated by reaction with O_2 produced by cyanobacteria (higher biomass iron formation) in shallow-waters; or oxidation of hydrothermal Fe(II) by anoxygenic photoferrotrophs or microaerophilic chemolithoautotrophs, followed by complete reduction by bacterial dissimilatory iron reduction (Konhauser et al., 2005; Johnson et al., 2008; Köhler et al., 2013) or by iron-mediated anaerobic methane-oxidizers (Konhauser et al., 2005; Sivan et al., 2011; Antler et al., 2015). Therefore, combining $\delta^{13}C_{org}$ with $\delta^{34}S$ and $\Delta^{33}S$, we hypothesize an early Neoproterozoic connection between the carbon and sulfur cycles.

The $\delta^{13}C_{org}$ excursion, with variations of more than 30‰, in the RDV BIF are contemporaneous and similar to excursions recorded in sedimentary sequences from Western Australia and South Africa (Thomazo et al., 2009a; Zerkle et al., 2012). Such negative excursions in $\delta^{13}C_{org}$ are often interpreted to reflect increased incorporation of ^{13}C -depleted methane into sedimentary organic matter through methanotrophy (using oxygen, sulfate, nitrate, or Mn-Fe oxide respiration; Hinrichs, 2002; Zerkle et al., 2012; Marin-Carbonne et al., 2018; Lepot et al., 2019). Although the lowest $\delta^{13}C_{org}$ values (-44‰ to -31‰), between 114 and 101 m core depth, in RDV are generally higher than those reported in other Neoproterozoic sequences (e.g., -60‰ ; Schirmer et al., 2016), they all coincide with near-zero or negative $\Delta^{33}S$ (0.4‰ to -0.7‰) and low $\delta^{34}S$ (2.7‰ to -3.1‰). The small S-MIF and slightly negative $\Delta^{33}S$ (indicating the availability of photolytic sulfate) and $\delta^{34}S$ (indicating sulfate reduction) suggest that the atmosphere was likely anoxic, and sulfate was available, but not abundant, as an oxidant in the water column (as expected for the anoxic Archean water column, Canfield et al., 2000; Habicht et al., 2002; Pavlov and Kasting, 2002; Ono et al., 2003). Anaerobic oxidation of methane using sulfate (SO_4^{2-} – AOM; Hinrichs, 2002) or iron (Fe – AOM; Sivan et al., 2011) as an electron acceptor during deposition and burial of methanotrophic derived biomass could produce the low $\delta^{13}C_{org}$ (< -30‰) observed in the BIF.

The relatively small magnitude S-MIF values throughout the BIF ($\Delta^{33}S = -0.7\text{‰}$ to 2.6‰) in RDV are similar to those observed in pyrites ($\Delta^{33}S = -1.0\text{‰}$ to 0.9‰) of the temporally equivalent Jeerinah (~2.6 Ga, average $\delta^{13}C_{org} -40.2\text{‰}$) and Tumbiana (~2.72 Ga, average $\delta^{13}C_{org} -39.3\text{‰}$) formations within the Pilbara Craton of Western Australia (Williford et al., 2016). The processes that influence the magnitude and sign of S-MIF remain equivocal. A discrete or early atmospheric O_2 increase (Kurzwil et al., 2013) or the effect of decreased photolysis within a thickened organic haze (Ueno et al., 2006; Domagal-Goldman et al., 2008; Thomazo et al., 2009a; Zerkle et al., 2012; Williford et al., 2016) are mechanisms commonly invoked to explain dampened S-MIF. Sampling and preservation biases in the sulfur isotopic record could explain anomalous changes in $\Delta^{33}S$ values (Claire et al., 2014). Relatively poor data-coverage of near-zero $\Delta^{33}S$ values from sequences around 2.7 Ga (Selvaraja et al., 2019), with the record mainly developed from cratons of South Africa (Kaapvaal Craton; Farquhar et al., 2007) and Western Australia (Pilbara Craton;

Ohmoto et al., 2006; Farquhar et al., 2007; Kaufman et al., 2007; Thomazo et al., 2009a) may provide an incomplete view of the Archean biosphere.

Although atmospheric sulfur chemistry was likely the main input to Archean seawater, an active prokaryotic sulfur cycle within the seafloor might greatly affect S-MIF preservation. Retention of $\Delta^{33}\text{S}$ photolytic sulfur fractionation from different carriers (S^0 with positive values or SO_4^{2-} with negative values) is favored by rapid pyrite formation when reduced sulfur species are available in the surficial sediments above the sulfate-methane transition zone (Halevy et al., 2010; Halevy, 2013). However, when pyrite forms late, dilution of the original photolytic fractionation by mixing between S-MIF carriers or biological fractionation tends to homogenize $\Delta^{33}\text{S}$ values (Halevy et al., 2010; Farquhar et al., 2013; Halevy, 2013).

Here we offer an explanation for two common features of the Meso and early Neoproterozoic sedimentary record (dampened $\Delta^{33}\text{S}$ values and Fe-carbonate-rich BIF) based on observations of early marine diagenesis in modern anoxic sediments (Liu et al., 2020a, 2020b). We propose that the high concentration of Fe_{Carb} relative to Fe_{Oxi} , low $\delta^{13}\text{C}_{\text{Org}}$, and near-zero $\Delta^{33}\text{S}$ values in the RDV BIF (Fig. 10) are evidence for Fe-AOM for the reasons that follow. First, Fe-AOM redistributes Fe(III) into Fe(II) mineral phases. In modern anoxic sediments, Fe(II) is generated by methane oxidation from Fe_{Oxi} precursors without significant decreases in methane concentrations (Sivan et al., 2011). In the Archean anoxic oceans, Fe(III) produced by photoferrotrophs in the water column or near the sediment-water interface could sustain Fe-AOM (Roland et al., 2021). Such reactions occur below the sulfate-methane transition in deep-sea sediments where sulfide (and sulfate) concentrations are low (Sivan et al., 2011; Riedinger et al., 2014) and likely closer to the sediment-water interface in the sulfate-limited Archean ocean. In modern sediments, late formed pyrite at the sulfate-methane transition zone has near-zero $\Delta^{33}\text{S}$ (0.05‰; Liu et al., 2020b). In the Archean ocean, late pyrite could most likely be mediated by Fe-AOM. Dampened S-MIF in RDV BIF might indicate that Fe (II) is becoming available (by Fe-AOM) for pyrite formation below the sulfate-methane zone, away from the sulfide production zone, and therefore undergo homogenization with biological sulfur fractionation and mixing between sulfur carriers with opposite isotopic values. Small euhedral habit pyrite (< 20 μm to < 50 μm) observed within the BIF also corroborates that they were formed later. The quartz content observed in the thin section (Fig. 4) and the abundance of iron carbonates in the RDV BIF suggest unfavorable conditions for dissimilatory iron reduction. In experimental observations under conditions of high dissolved silica and alkaline (pH = 8.7) waters, hematite reduction by dissimilatory iron reducers was significantly inhibited (Wu et al., 2009). If correct, Fe-AOM may have been optimized for Fe(III) reduction in silica and iron-rich waters.

Since anaerobic methanotrophy and an early organic haze were contemporaneous (Havig et al., 2017), both processes may have contributed to small S-MIF values in the RDV BIF. However, RDV represents the São Francisco Craton, which at 2.7 Ga is thought to be separated from the cratons forming the Vaalbara or Super-vaalbara supercontinents (Cheney, 1996; Wit, 1998; de Kock et al., 2009; Gumsley et al., 2017), and therefore minimizes the potential for sampling bias. Diagenetic reactions associated with active sulfur cycling triggered by nascent oxygen production (and thus sulfate production) have been identified as processes that may mix and unmix S-MIF signatures (Farquhar and Wing, 2003; Halevy, 2013). We suggest that similar anaerobic reactions observed in modern methane-rich sediments also have the potential for dampening S-MIF in bulk pyrite and should be addressed in future investigations.

Relatively higher organic matter content (TOC up to 7.8%) at low graphitization level (Fig. 8) and higher $\delta^{13}\text{C}_{\text{Org}}$ (−33.4‰ to −19.2‰)

coincide with an expansion in S-MIF ($\Delta^{33}\text{S} = 2.3\text{‰} \pm 0.8\text{‰}$) within the black shale above the BIF, indicating a change in environmental conditions. Sulfate levels probably remained limited, as supported by consistent positive $\delta^{34}\text{S}$ (from 0.5‰ to 7‰). Organic-rich shales, such as the RDV black shale, commonly overlying iron formations in Meso and Neoproterozoic sequences, reflect changes in primary productivity rates (Bekker et al., 2010). We argue for this explanation here.

Petrography and geochemistry suggest that Fe_{Py} (2.4%–88% of Fe_T) and Fe_{Carb} (9.5%–73% of Fe_T) contributions within the black shale varied considerably, but a few intervals are significantly enriched in small disseminated sulfides (Figs. 5 and 11). When considered with the higher $\delta^{13}\text{C}_{\text{Org}}$, this scenario may indicate diminished incorporation of ^{13}C -depleted methane into sedimentary organic matter through methanotrophy, implying lower methanogenesis (less efficient in organic matter mineralization; Canfield et al., 2018) and an increase in sulfide oxidation by anoxygenic phototrophic bacteria. Such biotic titration of Fe, shifting the basin from ferruginous to euxinic conditions, has been proposed by Johnston et al. (2010) and Canfield et al. (2018). Likely the organic matter, strongly positively correlated with Mo (Supplementary Data, Fig. S1), and pyrite contents in the RDV black shales record euxinic conditions and potentially a shallow depositional basin, although iron speciation is not conclusive (Fig. 10; Supplementary Data, Table S2). This scenario would explain the higher $\delta^{13}\text{C}_{\text{Org}}$ when compared to the BIF, reflecting lower incorporation of volatile organic matter such as methane and a greater contribution from anoxygenic phototrophic bacteria as the primary producers.

The change in $\delta^{13}\text{C}_{\text{Org}}$ coincides with an increase in the range of S-MIF, towards positive $\Delta^{33}\text{S}$ values, in the black shale (Fig. 10), which contrasts with the dampened values in the BIF. Such an expansion in $\Delta^{33}\text{S}$ values is also observed in pyrite from other Neoproterozoic records (e.g., Domagal-Goldman et al., 2008; Fakhraee et al., 2018). As Mesoarchean dampened S-MIF can be associated with an atmospheric organic-rich haze, the Neoproterozoic expansion can be related to its collapse (e.g., Zahnle et al., 2006; Domagal-Goldman et al., 2008; Zerkle et al., 2012) or intensification of volcanic SO_2 inputs (Philippot et al., 2012; Thomazo et al., 2013), increasing UV photolysis. Another possibility to explain higher positive $\Delta^{33}\text{S}$ would be a consequence of progressive seawater oxygenation and oxidative sulfur cycling during early diagenesis (e.g., Fakhraee et al., 2018).

Therefore, our dataset might be non-specific about the processes that resulted in the larger range of S-MIF. Considering that redox sulfur cycling between S^0 and sulfate pools was limited in the late Archean ocean (Ono et al., 2009a), and moderate amounts of CH_4 form more S^0 aerosols (DeWitt et al., 2010), it is reasonable to argue for a decrease of organic haze. Furthermore, as mentioned before, changes in $\Delta^{33}\text{S}$ could also be explained by mixing sulfur derived from biogenic and photolytic reactions (Farquhar et al., 2013). Since the RDV black shale was potentially deposited in euxinic conditions (and therefore with higher availability of sulfide), the lack of evidence for strong sulfate-reduction (positive $\delta^{34}\text{S}$) could indicate early pyrite formation. In this case, sulfur for pyrite formation might be provided by polysulfide derived from an elemental sulfur precursor preserving higher $\Delta^{33}\text{S}$ positive values (e.g., Farquhar et al., 2013).

Evolving environmental changes are also suggested by a second shift in the isotopic data ($\delta^{13}\text{C}_{\text{Org}}$, $\Delta^{33}\text{S}$, and $\delta^{34}\text{S}$) and iron mineral distribution, in the upper portion of the black shale and throughout the metasandstone (Fig. 10). We interpret a transition to a more stable ecology based on small-scale variation in $\delta^{13}\text{C}_{\text{Org}}$, which is most apparent at 50 m depth to the top of the core (Fig. 10). Values of $\delta^{13}\text{C}_{\text{Org}}$ between −30‰ and −25‰ are highly indicative of fractionation associated with the RuBisCO I enzyme (Schidlowski, 2001), consistent with carbon fixation by anoxygenic or oxygenic

photosynthesis (Schirmer et al., 2016). When coupled with the sulfur isotopic composition of pyrite, we suggest that a change in the primary producer community drove a local increase in oxygen production that exceeded the reducing sink, which coincides with the attenuation of S-MIF. The positive and almost uniform $\delta^{34}\text{S}$ pyrite values (average = $3.3\text{‰} \pm 0.5\text{‰}$) suggest environmental stability with low sulfate concentrations.

The transition to S-MDF, $\Delta^{33}\text{S} = 0 \pm 0.2\text{‰}$, in Archean sedimentary pyrite reflects atmospheric oxygen levels that are greater than 10^{-5} PAL, and the diminishment of UV-photolysis of volcanogenic SO_2 (e.g., Farquhar et al., 2000; Farquhar and Wing, 2003; Ueno, 2014; Fakrae et al., 2018). However, contact and inclusion of mantle sulfur could mute the magnitudes of primary $\delta^{34}\text{S}$ and $\Delta^{33}\text{S}$ (Fiorentini et al., 2012) and convolute paleoenvironmental interpretations. Pyrite with low $\Delta^{33}\text{S}$ (e.g., 0.27‰ to 3.46‰), from Archean gold deposits where hydrothermal processes dilute the original values (Fiorentini et al., 2012) are commonly reported (Ribeiro et al., 2015; Gregory et al., 2016; Kresse et al., 2018). The possibility that bulk pyrite sulfur isotopic values can include mixed sources of sulfides needs to be considered in the RDV quartz vein sequence.

If mantle sulfur signatures overprinted RDV sedimentary pyrite $\Delta^{33}\text{S}$, we should expect the potential mix of atmospheric S-MIF and S-MDF signatures superimposed by sulfur reactions in the hydrosphere that are exclusively mass-dependent (Ono et al., 2009a, 2009b). In this scenario, the relationship between the two minor sulfur isotopes ($\Delta^{33}\text{S}$ and $\Delta^{36}\text{S}$) works as a conservative proxy for Archean atmospheric S-MIF signatures (Farquhar et al., 2001, 2007; Ono et al., 2006b; Kaufman et al., 2007). Different arrays were proposed to differentiate S-MDF (e.g., the slope of ~ -6.8 , Ono et al., 2006b) and S-MIF (e.g., slope ~ -0.9 , for the Neoproterozoic, Ono et al., 2006b; Farquhar et al., 2007; Johnston, 2011). However, more recent work suggests that deviation from the Neoproterozoic array (also known as the Archean Array) to different slopes implies a change in either atmospheric chemistry or mixing between atmospheric sulfur sources (Zerkle et al., 2012).

For this comparison, we analyzed the paired $\Delta^{33}\text{S}$ and $\Delta^{36}\text{S}$ compositions of pyrite from the RDV BIF (one with positive and another negative $\Delta^{33}\text{S}$), black shale (the most positive $\Delta^{33}\text{S}$ value), and metasandstone (near zero, after the $\delta^{13}\text{C}_{\text{org}}$ reached a constant $< -30\text{‰}$ composition). The BIF and black shale samples followed the array expected for the Neoproterozoic (~ -0.9 , Fig. 12), indicating a S-MIF signal produced by coupled SO_2 photolysis and photo-

excitation (Ono, 2017). The metasandstone sample at 50.4 m depth has values near the origin (within analytical error) and could follow any slope intercepting it. We acknowledge the complexity of interpreting up-core variability in RDV using bulk sulfur isotope analysis and consider that the primary lithostratigraphy signatures could be potentially overprinted by juvenile and magmatic sulfur during hydrothermal and metamorphism, a well-known challenge to interpreting the Archean S-MIF record (Farquhar et al., 2000; Farquhar and Wing, 2003; Jamieson et al., 2006; Labidi et al., 2013; Roerdink et al., 2016; Selvaraja et al., 2017; Fiorentini et al., 2018; LaFlamme et al., 2018). Three alternative interpretations may explain the shift to near-zero $\Delta^{33}\text{S}$ in the bulk sulfides considering the cooccurring diagenetic and epigenetic pyrite in the upper black shale and the placement of the quartz vein between 68.5 and 69 m in the metasandstone: (i) hydrothermal overprint, (ii) an increase in oxygen production, and (iii) a mixed signature of both processes.

Monotonic and positive $\delta^{34}\text{S}$ accompanied with near-zero $\Delta^{33}\text{S}$ values could result from a complete overprint of primary signatures by another single sulfur source such as the mantle (e.g., Farquhar and Wing, 2003; Fiorentini et al., 2018). However, petrology and hydrothermal alteration assessments indicate these are highly localized effects (see section 5.1) proximal to the quartz vein within the lower metasandstone (Fig. 6). Furthermore, if a mantle source had overprinted the primary sulfur isotope record, it is difficult to reconcile why the same monotonic behavior is also observed with the $\delta^{13}\text{C}_{\text{org}}$ (ca. -34‰ , Fig. 10), especially in the upper 50 m of the core, that is ~ 20 m from the quartz vein. We suggest that near-zero $\Delta^{33}\text{S}$ reflects oxygen production during this prolonged period of ecosystem stability within the basin. This interpretation will benefit from further investigations of multiple sulfur isotopes in individual pyrite grains.

Therefore, given the mineralization context, a conservative approach is to consider that those isotopic signatures from 20 m below and above the quartz vein that have more variable $\Delta^{33}\text{S}$ (from -0.04‰ to 0.38‰) and $\delta^{13}\text{C}_{\text{org}}$ (-35.7‰ to -18.4‰), may represent a mix of sulfur sources (potentially, mantellic, photolytic, and mass-dependent). Considering that, it is still possible that within the metasandstone, sedimentary pyrite records a more active oxidative sulfur cycle linked to oxygen production by oxygenic photosynthesis ($\delta^{13}\text{C}_{\text{org}} = -30\text{‰}$). This process would result in Neoproterozoic pyrite overprinted by mass-dependent processes during the biological production of sulfide. Therefore, we suggest that the RDV record represents a transient episode of S-MIF attenuation in the sedimentary record, most likely due to the localized production of oxygen in the water column. S-MIF reported for pyrites in stratigraphically correlated formations within the Nova Lima Group sequence supports this interpretation. The observations of S-MIF in stratigraphically older Cuiabá deposit ($\Delta^{33}\text{S} = 1.6\text{‰} \pm 0.2\text{‰}$; Bühn et al., 2012, and $\Delta^{33}\text{S} = -0.47\text{‰} \pm 0.3\text{‰}$; Kresse et al., 2018) and the relatively younger Córrego do Sítio Formation ($\Delta^{33}\text{S} = 1.7\text{‰} \pm 0.1\text{‰}$; Ribeiro et al., 2015) suggest that a secondary pervasive fluid-related process cannot explain the absence of a S-MIF signal in RDV.

This pattern corroborates observations of short-duration episodes of S-MIF attenuation prior to the GOE (Philippot et al., 2018). Sulfur isotopic data throughout sections of the 2.7 Ga to 2.9 Ga timespan in the Pilbara Craton, Western Australia (Ohmoto et al., 2006), supports the observation that the level of atmospheric oxygen fluctuated considerably during the Archean era (Steadman et al., 2020) and that the preservation of the rare sulfur isotope record might be affected by the contemporaneous biosphere.

To our knowledge, there is no previous evidence of early oxygenation or oxygen oasis described for the Rio das Velhas Greenstone Belt. Two studies indicate free molecular oxygen, before

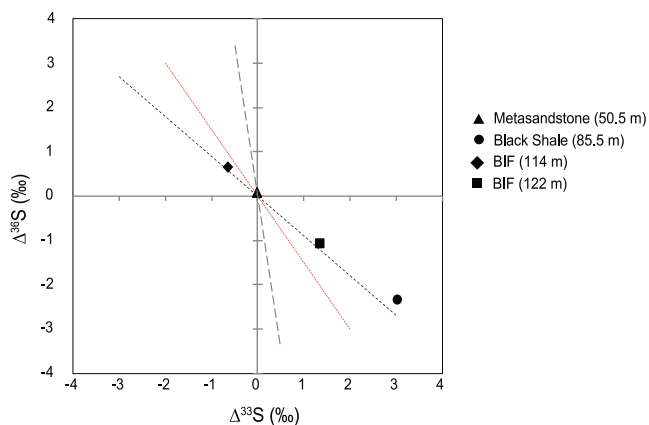


Fig. 12. $\Delta^{36}\text{S}$ vs. $\Delta^{33}\text{S}$ values for representative lithologies of the RDV core, including metasandstone (50.5 m, triangle), black shale (85.5 m; circle), and BIF-chert (114 and 122 m; diamond and square, respectively). The red array from Zerkle et al. (2012); the black dotted array represents the relationship expected for Neoproterozoic S-MIF ($m \sim -0.9$; Farquhar et al., 2007), and the gray dashed array represents S-MDF ($m \sim -6.8$; Ono et al., 2006b).

the GOE, in the sedimentary record of the Pitangui Greenstone Belt (Brando Soares et al., 2017; Bosco-Santos et al., 2020) to the west in the Quadrilátero Ferrífero. Traditionally these Greenstone Belts have been considered to represent a single Archean basin, but recently, it has been shown that they represent distinct basins (Brando Soares et al., 2017; Melo-Silva et al., 2020). The evidence of early oxygen production (Brando Soares et al., 2017; Bosco-Santos et al., 2020) in the adjacent basin with minimum depositional age at 2.69 Ga (Melo-Silva et al., 2020) corroborates our interpretation for localized early oxygenation.

6. Closing statement and future perspectives

Here we show evidence for local biogeochemistry changes and oxygen production approximately 300 Ma before the GOE that influenced S-MIF preservation. Although the current data coverage suggests a global history of S-MIF dynamics throughout the Archean, the range and magnitude of $\Delta^{33}\text{S}$ fractionation are represented mainly by two cratons, the Kaapvaal and Pilbara (Fig. 1). By consensus, those terrains retain well-preserved, low metamorphic grade sequences; however, the analytical advances allow us today to delineate the extent of post-depositional alteration. This opens a new window for exploring different Archean terrains that can help build a more complete perspective of S-MIF dynamics and the timing of oxygenation from the heterogeneous global record. Contrary to Western Australia and South Africa Cratons, where dampened isotopic variability preceded a broader range in $\Delta^{33}\text{S}$ values, the São Francisco Craton shows small variations, during the entire Archean, with the median around $0 \pm 2\text{‰}$. The Zimbabwe and North China Cratons also show medians around $0 \pm 1\text{‰}$, and low data coverage from Amazon and Dwarwar Cratons points to similar ranges. Dampened S-MIF in the RDV BIF, representing the São Francisco Craton, can correspond to the traditional dampened values for Meso to early Neoproterozoic (3.2–2.72 Ga) sequences in Kaapvaal and Pilbara Cratons (-4‰ to 1.9‰ , Ohmoto et al., 2006; Ono et al., 2006a; Farquhar et al., 2007; Domagal-Goldman et al., 2008; Thomazo et al., 2009a; Guy et al., 2012; Izon et al., 2015; Williford et al., 2016; Liu, L. et al., 2020c). Here, however, we discuss the possibility that besides spatial sampling bias, S-MIF preservation should be considered in parallel with the Archean biosphere. The enigmatic secular record of minor sulfur isotopes can give many clues into ancient Earth biogeochemistry, but it is necessary to expand it and interpret it in parallel with Archean geography.

Declaration of Competing Interest

The authors declare that they have no known competing financial interests or personal relationships that could have appeared to influence the work reported in this paper.

Acknowledgments

We thank São Paulo Research Foundation (FAPESP grants 2016/02933-2 to ABS, 12/15824-6 to EPO and 2015/16235-2 to PP) and the Agouron Institute (to WPG) for financial support. We also thank Jaguar Mining Co for technical and logistic support. Special thanks to Armando José Massucatto and Romulo Thiago Cruz for their assistance at Roça Grande mine. Thank you to Brooke Vander Pas (IUPUI) and Eric Haitt (University of Wisconsin-Oshkosh) for preparing the thin sections. We appreciate helpful comments and discussions with Wil Leavitt and Mariana Brando Soares that helped improve our interpretations. Comments and detailed revisions from Nivea Magalhães and an anonymous reviewer significantly improved the manuscript.

Appendix A. Supplementary data

Supplementary data to this article can be found online at <https://doi.org/10.1016/j.gsf.2021.101250>.

References

- Ague, J.J., Van Haren, J.L., 1996. Assessing metasomatic mass and volume changes using the bootstrap, with application to deep crustal hydrothermal alteration of marble. *Econ. Geol.* 91, 1169–1182.
- Alkmim, F.F., Marshak, S., 1998. Transamazonian orogeny in the Southern São Francisco craton region, Minas Gerais, Brazil: evidence for Paleoproterozoic collision and collapse in the Quadrilátero Ferrífero. *Precambrian Res.* 90, 29–58.
- Anbar, A.D., Duan, Y., Lyons, T.W., Arnold, G.L., Kendall, B., Creaser, R.A., Kaufman, A. J., Gordon, G.W., Scott, C., Garvin, J., 2007. A whiff of oxygen before the great oxidation event?. *Science* 317, 1903–1906.
- Antler, G., Turchyn, A.V., Herut, B., Sivan, O., 2015. A unique isotopic fingerprint of sulfate-driven anaerobic oxidation of methane. *Geology* 43, 619–622.
- Aoya, M., Kouketsu, Y., Endo, S., Shimizu, H., Mizukami, T., Nakamura, D., Wallis, S., 2010. Extending the applicability of the Raman carbonaceous-material geothermometer using data from contact metamorphic rocks. *J. Metamorph. Geol.* 28, 895–914.
- Araújo, J.C.S., Ferreira, R., Freitas, F., Magalhães, J., 2020a. The Archean Rio das Velhas greenstone belt revisited: new insights into the stratigraphy. *J. Geol. Surv. Brazil* 3, 113–149.
- Araújo, J.C.S., Lobato, L.M., 2019. Depositional model for banded iron formation host to gold in the Archean Rio das Velhas greenstone belt, Brazil, based on geochemistry and LA-ICP-MS magnetite analyses. *J. South Am. Earth Sci.* 94, 102205. [10.1016/j.jsames.102019.102205](https://doi.org/10.1016/j.jsames.102019.102205).
- Araújo, J.C.S., Ribeiro, J.H., Tuller, M.P., Signorelli, N., 2020b. Carta geológica e de recursos minerais da folha Gandarela (SE. 23-XA-III-2-NO): Quadrilátero Ferrífero (in Portuguese).
- Baltazar, O., Silva, S., 1996. Projeto Rio das Velhas: Mapa Geológico Integrado do Supergrupo Rio das Velhas, escala 1: 100.000. *Braz. Geol. Surv. - CPRM* (in Portuguese).
- Baltazar, O., Baars, F., Lobato, L., Reis, L., Achtschin, A., Berni, G., Silveira, V., 2005. Mapa geológico do Quadrilátero Ferrífero na escala 1: 50.000 com nota explicativa. CODEMIG (in Portuguese).
- Baltazar, O., Zucchetti, M., 2007. Lithofacies associations and structural evolution of the Archean Rio das Velhas greenstone belt, Quadrilátero Ferrífero, Brazil: a review of the setting of gold deposits. *Ore Geol. Rev.* 32, 471–499.
- Bekker, A., Holland, H., Wang, P.-L., Rumble, D., Stein, H., Hannah, J., Coetzee, L., Beukes, N., 2004. Dating the rise of atmospheric oxygen. *Nature* 427, 117–120.
- Bekker, A., Slack, J.F., Planavsky, N., Krapez, B., Hofmann, A., Konhauser, K.O., Rouxel, O.J., 2010. Iron formation: the sedimentary product of a complex interplay among mantle, tectonic, oceanic, and biospheric processes. *Econ. Geol.* 105, 467–508.
- Beny-Bassez, C., Rouzaud, J., 1984. Characterization of carbonaceous materials by correlated electron and optical microscopy and raman microspectroscopy. *Scan. Electron Microsc.* 1985, 11.
- Beysac, O., Goffé, B., Chopin, C., Rouzaud, J., 2002. Raman spectra of carbonaceous material in metasediments: a new geothermometer. *J. Metamorph. Geol.* 20, 859–871.
- Bleeker, W., 2003. The late Archean record: a puzzle in ca. 35 pieces. *Lithos* 71, 99–134.
- Bosco-Santos, A., Gilhooly III, W.P., Fouskas, F., Fabricio-Silva, W., Oliveira, E.P., 2020. Euxinia in the Neoproterozoic: The starting point for early oxygenation in a Brazilian Craton. *Precambrian Res.* 341, 105655. [10.1016/j.precamres.102020.105655](https://doi.org/10.1016/j.precamres.102020.105655).
- Brando Soares, M., Neto, A.V.C., Fabricio-Silva, W., 2020. The development of a Meso-to Neoproterozoic rifting-convergence-collision-collapse cycle over an ancient thickened protocontinent in the south São Francisco craton, Brazil. *Gondwana Res.* 77, 40–66.
- Brando Soares, M.N., Corrêa, A.V., Zeh, A., Cabral, A.R., Pereira, L.F., do Prado, M.G.B., de Almeida, A.M., Manduca, L.G., da Silva, P.H.M., de Araújo Mabub, R.O., 2017. Geology of the Pitangui greenstone belt, Minas Gerais, Brazil: stratigraphy, geochronology and BIF geochemistry. *Precambrian Res.* 291, 17–41.
- Bucher, K., Grapes, R., 2011. *Petrogenesis of Metamorphic Rocks*. Springer Science & Business Media.
- Bühn, B., Santos, R.V., Dardenne, M.A., de Oliveira, C.G., 2012. Mass-dependent and mass-independent sulfur isotope fractionation ($\delta^{34}\text{S}$ and $\delta^{33}\text{S}$) from Brazilian Archean and Proterozoic sulfide deposits by laser ablation multi-collector ICP-MS. *Chem. Geol.* 312, 163–176.
- Buseck, P.R., Beysac, O., 2014. From organic matter to graphite: Graphitization. *Elements* 10, 421–426.
- Canfield, D.E., Habicht, K.S., Thamdrup, B., 2000. The Archean sulfur cycle and the early history of atmospheric oxygen. *Science* 288, 658–661.
- Canfield, D.E., Raiswell, R., Westrich, J.T., Reaves, C.M., Berner, R.A., 1986. The use of chromium reduction in the analysis of reduced inorganic sulfur in sediments and shales. *Chem. Geol.* 54, 149–155.
- Canfield, D.E., Zhang, S., Wang, H., Wang, X., Zhao, W., Su, J., Bjerrum, C.J., Haxen, E. R., Hammarlund, E.U., 2018. A Mesoproterozoic iron formation. *Proc. Natl. Acad. Sci. U.S.A.* 115, E3895–E3904.

- Caruso, S., Fiorentini, M.L., Hollis, S.P., LaFlamme, C., Baumgartner, R.J., Steadman, J.A., Savard, D., 2018. The fluid evolution of the Nimbus Ag-Zn-(Au) deposit: an interplay between mantle plume and microbial activity. *Precambrian Res.* 317, 211–229.
- Chang, S.-B.R., Kirschvink, J.L., 1985. Possible biogenic magnetite fossils from the Late Miocene Potamida clays of Crete. In: Kirschvink, J.L., Jones, D.S., MacFadden, B.J. (Eds.), *Magnetite Biomineralization and Magnetoreception in Organisms*. Topics in Geobiology, vol 5. Springer, Boston, MA, pp. 647–669. 10.1007/978-1-4613-0313-8_36.
- Chen, M., Campbell, I.H., Xue, Y., Tian, W., Ireland, T.R., Holden, P., Cas, R.A., Hayman, P.C., Das, R., 2015. Multiple sulfur isotope analyses support a magmatic model for the volcanogenic massive sulfide deposits of the Teutonic Bore Volcanic Complex, Yilgarn Craton, Western Australia. *Econ. Geol.* 110, 1411–1423.
- Cheney, E., 1996. Sequence stratigraphy and plate tectonic significance of the Transvaal succession of southern Africa and its equivalent in Western Australia. *Precambrian Res.* 79, 3–24.
- Claire, M.W., Kasting, J.F., Domagal-Goldman, S.D., Stüeken, E.E., Buick, R., Meadows, V.S., 2014. Modeling the signature of sulfur mass-independent fractionation produced in the Archean atmosphere. *Geochim. Cosmochim. Acta* 141, 365–380.
- Cline, J.D., 1969. Spectrophotometric determination of hydrogen sulfide in natural waters 1. *Limnol. Oceanogr.* 14, 454–458.
- Cox, J., Pressacco, R., 2016. Technical Report on the Roça Grande and Pilar Mines, Minas Gerais State, Jaguar Mining Company, Brazil.
- Crowe, S.A., Dössing, L.N., Beukes, N.J., Bau, M., Kruger, S.J., Frei, R., Canfield, D.E., 2013. Atmospheric oxygenation three billion years ago. *Nature* 501, 535–538.
- Cutts, K., Lana, C., Alkmim, F., Farina, F., Moreira, H., Coelho, V., 2019. Metamorphism and exhumation of basement gneiss domes in the Quadrilátero Ferrífero: two stage dome-and-keel evolution? *Geosci. Front.* 10, 1765–1787.
- da Silva, L.C., Noce, C.M., Lobato, L.M., 2017. Dacitic volcanism in the course of the Rio Das Velhas (2800–2690 Ma) Orogeny: a Brazilian Archean Analogue (TTD) to the modern adakites. *Brazilian J. Geol.* 30, 384–387.
- de Kock, M.O., Evans, D.A., Beukes, N.J., 2009. Validating the existence of Vaalbara in the Neoproterozoic. *Precambrian Res.* 174, 145–154.
- DeWitt, H.L., Hasenkopf, C.A., Trainer, M.G., Farmer, D.K., Jimenez, J.L., McKay, C.P., Toon, O.B., Tolbert, M.A., 2010. The formation of sulfate and elemental sulfur aerosols under varying laboratory conditions: implications for early Earth. *Astrobiology* 10, 773–781.
- Ding, T., Valkiers, S., Kipphardt, H., De Bievre, P., Taylor, P., Gonfiantini, R., Krouse, R., 2001. Calibrated sulfur isotope abundance ratios of three IAEA sulfur isotope reference materials and V-CDT with a reassessment of the atomic weight of sulfur. *Geochim. Cosmochim. Acta* 65, 2433–2437.
- Domagal-Goldman, S.D., Kasting, J.F., Johnston, D.T., Farquhar, J., 2008. Organic haze, glaciations and multiple sulfur isotopes in the Mid-Archean Era. *Earth Planet. Sci. Lett.* 269, 29–40.
- Dopico, C.I.M., Lana, C., Moreira, H.S., Cassino, L.F., Alkmim, F.F., 2017. U-Pb ages and Hf-isotope data of detrital zircons from the late Neoproterozoic-Paleoproterozoic Minas Basin, SE Brazil. *Precambrian Res.* 291, 143–161.
- Fabre, S., Nédélec, A., Poitrasson, F., Strauss, H., Thomazo, C., Nogueira, A., 2011. Iron and sulphur isotopes from the Carajás mining province (Pará, Brazil): Implications for the oxidation of the ocean and the atmosphere across the Archean-Proterozoic transition. *Chem. Geol.* 289, 124–139.
- Fakhraee, M., Crowe, S.A., Katsev, S., 2018. Sedimentary sulfur isotopes and Neoproterozoic ocean oxygenation. *Sci. Adv.* 4, e1701835. 1701810.1701126/sciadv.1701835.
- Farina, F., Albert, C., Lana, C., 2015. The Neoproterozoic transition between medium- and high-K granitoids: Clues from the Southern São Francisco Craton (Brazil). *Precambrian Res.* 266, 375–394.
- Farquhar, J., Bao, H., Thiemens, M., 2000. Atmospheric influence of Earth's earliest sulfur cycle. *Science* 289, 756–758.
- Farquhar, J., Cliff, J., Zerkle, A.L., Kamysny, A., Poulton, S.W., Claire, M., Adams, D., Harms, B., 2013. Pathways for Neoproterozoic pyrite formation constrained by mass-independent sulfur isotopes. *Proc. Natl. Acad. Sci. U.S.A.* 110, 17638–17643.
- Farquhar, J., Peters, M., Johnston, D.T., Strauss, H., Masterson, A., Wiechert, U., Kaufman, A.J., 2007. Isotopic evidence for Mesoarchean anoxia and changing atmospheric sulphur chemistry. *Nature* 449, 706–709.
- Farquhar, J., Savarino, J., Airieau, S., Thiemens, M.H., 2001. Observation of wavelength-sensitive mass-independent sulfur isotope effects during SO₂ photolysis: implications for the early atmosphere. *J. Geophys. Res. Planets* 106, 32829–32839.
- Farquhar, J., Wing, B.A., 2003. Multiple sulfur isotopes and the evolution of the atmosphere. *Earth Planet. Sci. Lett.* 213, 1–13.
- Ferry, J.M., 1981. Petrology of graphitic sulfide-rich schists from south-central Maine: an example of desulfidation during prograde regional metamorphism. *Am. Mineral.* 66, 908–930.
- Florentini, M.L., Bekker, A., Rouxel, O., Wing, B.A., Maier, W., Rumble, D., 2012. Multiple sulfur and iron isotope composition of magmatic Ni-Cu-(PGE) sulfide mineralization from eastern Botswana. *Econ. Geol.* 107, 105–116.
- Florentini, M.L., LaFlamme, C., Denyszyn, S., Mole, D., Maas, R., Locmelis, M., Caruso, S., Bui, T.-H., 2018. Post-collisional alkaline magmatism as gateway for metal and sulfur enrichment of the continental lower crust. *Geochim. Cosmochim. Acta* 223, 175–197.
- Fischer, W.W., Fike, D.A., Johnson, J.E., Raub, T.D., Guan, Y., Kirschvink, J.L., Eiler, J.M., 2014. SQUID-SIMS is a useful approach to uncover primary signals in the Archean sulfur cycle. *Proc. Natl. Acad. Sci. U.S.A.* 111, 5468–5473.
- Floyd, P., Leveridge, B., 1987. Tectonic environment of the Devonian Gramscatho basin, south Cornwall: framework mode and geochemical evidence from turbiditic sandstones. *J. Geol. Soc.* 144, 531–542.
- Grant, J.A., 1986. The isocon diagram: a simple solution to Gresens' equation for metasomatic alteration. *Econ. Geol.* 81, 1976–1982.
- Gregory, D.D., Large, R.R., Bath, A.B., Steadman, J.A., Wu, S., Danyushevsky, L., Bull, S.W., Holden, P., Ireland, T.R., 2016. Trace element content of pyrite from the Kapii slate, St. Ives Gold District, Western Australia. *Econ. Geol.* 111, 1297–1320.
- Gregory, D.D., Large, R.R., Halpin, J.A., Steadman, J.A., Hickman, A.H., Ireland, T.R., Holden, P., 2015. The chemical conditions of the late Archean Hamersley basin inferred from whole rock and pyrite geochemistry with $\Delta^{33}\text{S}$ and $\delta^{34}\text{S}$ isotope analyses. *Geochim. Cosmochim. Acta* 149, 223–250.
- Gumslied, A.P., Chamberlain, K.R., Bleeker, W., Söderlund, U., de Kock, M.O., Larsson, E.R., Bekker, A., 2017. Timing and tempo of the Great Oxidation Event. *Proc. Natl. Acad. Sci. U.S.A.* 114, 1811–1816.
- Guo, Q., Strauss, H., Kaufman, A.J., Schröder, S., Gutzmer, J., Wing, B., Baker, M.A., Bekker, A., Jin, Q., Kim, S.-T., 2009. Reconstructing Earth's surface oxidation across the Archean-Proterozoic transition. *Geology* 37, 399–402.
- Guy, B., Ono, S., Gutzmer, J., Kaufman, A., Lin, Y., Fogel, M., Beukes, N., 2012. A multiple sulfur and organic carbon isotope record from non-conglomeratic sedimentary rocks of the Mesoarchean Witwatersrand Supergroup, South Africa. *Precambrian Res.* 216, 208–231.
- Guy, B., Ono, S., Gutzmer, J., Lin, Y., Beukes, N., 2014. Sulfur sources of sedimentary "buckshot" pyrite in the auriferous conglomerates of the Mesoarchean Witwatersrand and Ventersdorp Supergroups, Kaapvaal Craton, South Africa. *Miner. Depos.* 49, 751–775.
- Habicht, K.S., Gade, M., Thamdrup, B., Berg, P., Canfield, D.E., 2002. Calibration of sulfate levels in the Archean ocean. *Science* 298, 2372–2374.
- Halevy, I., 2013. Production, preservation, and biological processing of mass-independent sulfur isotope fractionation in the Archean surface environment. *Proc. Natl. Acad. Sci. U.S.A.* 110, 17644–17649.
- Halevy, I., Johnston, D.T., Schrag, D.P., 2010. Explaining the structure of the Archean mass-independent sulfur isotope record. *Science* 329, 204–207.
- Hauri, E.H., Papineau, D., Wang, J., Hillion, F., 2016. High-precision analysis of multiple sulfur isotopes using NanoSIMS. *Chem. Geol.* 420, 148–161.
- Havig, J.R., Hamilton, T.L., Bachan, A., Kump, L.R., 2017. Sulfur and carbon isotopic evidence for metabolic pathway evolution and a four-stepped Earth system progression across the Archean and Paleoproterozoic. *Earth-Sci. Rev.* 174, 1–21.
- Heilbron, M., Cordani, U.G., Alkmim, F.F., 2017. The São Francisco Craton and its Margins, São Francisco Craton, Eastern Brazil. Springer, pp. 3–13.
- Henry, D.G., Jarvis, I., Gillmore, G., Stephenson, M., 2019. Raman spectroscopy as a tool to determine the thermal maturity of organic matter: Application to sedimentary, metamorphic and structural geology. *Earth-Sci. Rev.* 198, 102936. 102910.101016/j.earscirev.102019.102936.
- Hinrichs, K.U., 2002. Microbial fixation of methane carbon at 2.7 Ga: Was an anaerobic mechanism possible? *Geochim. Geophys. Geosy.* 3, 1–10.
- Hofmann, A., Bekker, A., Rouxel, O., Rumble, D., Master, S., 2009. Multiple sulphur and iron isotope composition of detrital pyrite in Archean sedimentary rocks: a new tool for provenance analysis. *Earth Planet. Sci. Lett.* 286, 436–445.
- Holland, H.D., 2002. Volcanic gases, black smokers, and the Great Oxidation Event. *Geochim. Cosmochim. Acta* 66, 3811–3826.
- Hood, S.B., Cracknell, M.J., Gazley, M.F., Reading, A.M., 2019. Element mobility and spatial zonation associated with the Archean Hamlet orogenic Au deposit, Western Australia: implications for fluid pathways in shear zones. *Chem. Geol.* 514, 10–26.
- Hou, K., Li, Y., Wan, D., 2007. Constraints on the Archean atmospheric oxygen and sulfur cycle from mass-independent sulfur records from Anshan-Benxi BIFs, Liaoning Province, China. *Sci. China Earth Sci.* 50, 1471–1478.
- Hu, G., Rumble, D., Wang, P.-L., 2003. An ultraviolet laser microprobe for the in situ analysis of multisulfur isotopes and its use in measuring Archean sulfur isotope mass-independent anomalies. *Geochim. Cosmochim. Acta* 67, 3101–3118.
- Izon, G., Zerkle, A.L., Zhelezinskaia, I., Farquhar, J., Newton, R.J., Poulton, S.W., Eigenbrode, J.L., Claire, M.W., 2015. Multiple oscillations in Neoproterozoic atmospheric chemistry. *Earth Planet. Sci. Lett.* 431, 264–273.
- Jamieson, J.W., Wing, B.A., Hannington, M.D., Farquhar, J., 2006. Evaluating isotopic equilibrium among sulfide mineral pairs in Archean ore deposits: case study from the Kidd Creek VMS deposit, Ontario, Canada. *Econ. Geol.* 101, 1055–1061.
- Jehlička, J., Beny, C., 1999. First and second-order Raman spectra of natural highly carbonized organic compounds from metamorphic rocks. *J. Mol. Struct.* 480, 541–545.
- Johnson, C.M., Beard, B.L., Klein, C., Beukes, N.J., Roden, E.E., 2008. Iron isotopes constrain biologic and abiologic processes in banded iron formation genesis. *Geochim. Cosmochim. Acta* 72, 151–169.
- Johnson, C.M., Ludois, J.M., Beard, B.L., Beukes, N.J., Heimann, A., 2013. Iron formation carbonates: paleoceanographic proxy or recorder of microbial diagenesis? *Geology* 41, 1147–1150.
- Johnston, D.T., 2011. Multiple sulfur isotopes and the evolution of Earth's surface sulfur cycle. *Earth-Sci. Rev.* 106, 161–183.
- Johnston, D.T., Poulton, S.W., Dehler, C., Porter, S., Husson, J., Canfield, D.E., Knoll, A.H., 2010. An emerging picture of Neoproterozoic ocean chemistry: insights from the Chuar Group, Grand Canyon, USA. *Earth Planet. Sci. Lett.* 290, 64–73.
- Kamber, B., Whitehouse, M., 2007. Micro-scale sulphur isotope evidence for sulphur cycling in the late Archean shallow ocean. *Geobiology* 5, 5–17.
- Kaufman, A.J., Johnston, D.T., Farquhar, J., Masterson, A.L., Lyons, T.W., Bates, S., Anbar, A.D., Arnold, G.L., Garvin, J., Buick, R., 2007. Late Archean biospheric oxygenation and atmospheric evolution. *Science* 317, 1900–1903.

- Köhler, I., Konhauser, K.O., Papineau, D., Bekker, A., Kappler, A., 2013. Biological carbon precursor to diagenetic siderite with spherical structures in iron formations. *Nat. Commun.* 4, 1–7.
- Konhauser, K., Newman, D., Kappler, A., 2005. The potential significance of microbial Fe (III) reduction during deposition of Precambrian banded iron formations. *Geobiology* 3, 167–177.
- Kresse, C., Lobato, L.M., Hagemann, S.G., e Silva, R.C.F., 2018. Sulfur isotope and metal variations in sulfides in the BIF-hosted orogenic Cuibá gold deposit, Brazil: implications for the hydrothermal fluid evolution. *Ore Geol. Rev.* 98, 1–27.
- Kurzweil, F., Claire, M., Thomazo, C., Peters, M., Hannington, M., Strauss, H., 2013. Atmospheric sulfur rearrangement 2.7 billion years ago: evidence for oxygenic photosynthesis. *Earth Planet. Sci. Lett.* 366, 17–26.
- Labidi, J., Cartigny, P., Moreira, M., 2013. Non-chondritic sulphur isotope composition of the terrestrial mantle. *Nature* 501, 208–211.
- LaFlamme, C., Jamieson, J.W., Fiorentini, M.L., Thébaud, N., Caruso, S., Selvaraja, V., 2018. Investigating sulfur pathways through the lithosphere by tracing mass independent fractionation of sulfur to the Lady Bountiful orogenic gold deposit, Yilgarn Craton. *Gondwana Res.* 58, 27–38.
- Lalonde, S.V., Konhauser, K.O., 2015. Benthic perspective on Earth's oldest evidence for oxygenic photosynthesis. *Proc. Natl. Acad. Sci. U.S.A.* 112, 995–1000.
- Lana, C., Alkmim, F.F., Armstrong, R., Scholz, R., Romano, R., Nalini Jr, H.A., 2013. The ancestry and magmatic evolution of Archean TTG rocks of the Quadrilátero Ferrífero province, southeast Brazil. *Precambrian Res.* 231, 157–173.
- Lebrun, E., Thébaud, N., Miller, J., Roberts, M., Evans, N., 2017. Mineralisation footprints and regional timing of the world-class Siguiri orogenic gold district (Guinea, West Africa). *Miner. Depos.* 52, 539–564.
- Lepot, K., Williford, K.H., Philippot, P., Thomazo, C., Ushikubo, T., Kitajima, K., Mostefaoui, S., Valley, J.W., 2019. Extreme ¹³C-depletions and organic sulfur content argue for S-fueled anaerobic methane oxidation in 2.7 Ga old stromatolites. *Geochim. Cosmochim. Acta* 244, 522–547.
- Li, J., Zhang, Z., Stern, R.A., Hannah, J.L., Stein, H.J., Yang, G., Li, L., 2017. Primary multiple sulfur isotopic compositions of pyrite in 2.7 Ga shales from the Joy Lake sequence (Superior Province) show felsic volcanic array-like signature. *Geochim. Cosmochim. Acta* 202, 310–340.
- Liu, J., Pellerin, A., Antler, G., Kasten, S., Findlay, A.J., Dohrmann, I., Røy, H., Turchyn, A.V., Jørgensen, B.B., 2020a. Early diagenesis of iron and sulfur in Bornholm Basin sediments: The role of near-surface pyrite formation. *Geochim. Cosmochim. Acta* 284, 43–60.
- Liu, J., Pellerin, A., Izon, G., Wang, J., Antler, G., Liang, J., Su, P., Jørgensen, B.B., Ono, S., 2020b. The multiple sulphur isotope fingerprint of a sub-seafloor oxidative sulphur cycle driven by iron. *Earth Planet. Sci. Lett.* 536, 116165. [116110.1016/j.epsl.2020.116165](https://doi.org/10.1016/j.epsl.2020.116165).
- Liu, L., Ireland, T., Holden, P., 2020. In-situ quadruple sulfur isotopic compositions of pyrites in the ca. 3.2–2.7 Ga metasedimentary rocks from the Pilbara Craton, Western Australia. *Chem. Geol.* 557, 119837. [119810.1016/j.chemgeo.2020.119837](https://doi.org/10.1016/j.chemgeo.2020.119837).
- Lobato, L.M., Ribeiro-Rodrigues, L.C., Vieira, F.W.R., 2001. Brazil's premier gold province. Part II: geology and genesis of gold deposits in the Archean Rio das Velhas greenstone belt. *Quadrilátero Ferrífero. Miner. Depos.* 36, 249–277.
- Lobato, L.M., Vieira, F.W.R., Ribeiro-Rodrigues, L., Pereira, L., Menezes, M., Junqueira, P., Pereira, S., 1998. Styles of hydrothermal alteration and gold mineralization associated with the Nova Lima Group of the Quadrilátero Ferrífero: Part II, the Archean mesothermal gold-bearing hydrothermal system. *Brazilian J. Geol.* 28, 355–366.
- Ludwig, K., 2012. User's Manual for Isoplot Version 3.75–4.15: A Geochronological Toolkit for Microsoft Excel. 5. Berkley Geochronological Centre, Special Publication.
- Luo, G., Ono, S., Beukes, N.J., Wang, D.T., Xie, S., Summons, R.E., 2016. Rapid oxygenation of Earth's atmosphere 2.33 billion years ago. *Sci. Adv.* 2, e1600134. [1600110.1601126/sciadv.1600134](https://doi.org/10.1126/sciadv.1600134).
- Machado, N., Carneiro, M., 1992. U-Pb evidence of late Archean tectono-thermal activity in the southern São Francisco shield, Brazil. *Can. J. Earth Sci.* 29, 2341–2346.
- Machado, N., Noce, C., Ladeira, E., De Oliveira, O.B., 1992. U-Pb geochronology of Archean magmatism and Proterozoic metamorphism in the Quadrilátero Ferrífero, southern São Francisco craton, Brazil. *Geol. Soc. Am. Bull.* 104, 1221–1227.
- Machado, N., Noce, C., Oliveira, O.d., Ladeira, E., 1989. Evolução geológica do Quadrilátero Ferrífero no Arqueano e Proterozóico Inferior, com base em geocronologia U-Pb. *Simpósio de Geologia de Minas Gerais* 5, 1–5 (in Portuguese).
- Machado, N., Schrank, A., Noce, C., Gauthier, G., 1996. Ages of detrital zircon from Archean-Paleoproterozoic sequences: Implications for Greenstone Belt setting and evolution of a Transamazonian foreland basin in Quadrilátero Ferrífero, southeast Brazil. *Earth Planet. Sci. Lett.* 141, 259–276.
- Magaldi, T.T., Navarro, M.S., Enzweiler, J., 2019. Assessment of dissolution of silicate rock reference materials with ammonium bifluoride and nitric acid in a microwave oven. *Geostand. Geoanal. Res.* 43, 189–208.
- Marin-Carbonne, J., Remusat, L., Sforza, M.C., Thomazo, C., Cartigny, P., Philippot, P., 2018. Sulfur isotope's signal of nanopyrates enclosed in 2.7 Ga stromatolitic organic remains reveal microbial sulfate reduction. *Geobiology* 16, 121–138.
- Marinho, M., Silva, M., Lombello, J., Di Salvo, L., Silva, R., Fébilo, W., Brito, D., 2018. Mapa Geológico Integrado do Sinclínio Pitangui. Projeto ARIM-Áreas de Relevante Interesse Mineral-Noroeste do Quadrilátero Ferrífero (in Portuguese).
- Melo-Silva, P., da Silva Amaral, W., Oliveira, E.P., 2020. Geochronological evolution of the Pitangui greenstone belt, southern São Francisco Craton, Brazil: Constraints from U-Pb zircon age, geochemistry and field relationships. *J. South Am. Earth Sci.* 99, 102380. [102310.1016/j.jsames.2020.102380](https://doi.org/10.1016/j.jsames.2020.102380).
- Mishima, K., Yamazaki, R., Satish-Kumar, M., Ueno, Y., Hokada, T., Toyoshima, T., 2017. Multiple sulfur isotope geochemistry of Dharwar Supergroup, Southern India: Late Archean record of changing atmospheric chemistry. *Earth Planet. Sci. Lett.* 464, 69–83.
- Moreira, H., Lana, C., Nalini Jr, H.A., 2016. The detrital zircon record of an Archean convergent basin in the Southern São Francisco Craton, Brazil. *Precambrian Res.* 275, 84–99.
- Moreira, H., Cassino, L., Lana, C., Storey, C., Albert, Capucine, 2019. Insights into orogenic process from drab schists and minor intrusions: Southern São Francisco Craton. Brazil. *Lithos* 346–347. <https://doi.org/10.1016/j.lithos.2019.07.013> 105146.
- Muller, É., Philippot, P., Rollion-Bard, C., Cartigny, P., 2016. Multiple sulfur-isotope signatures in Archean sulfates and their implications for the chemistry and dynamics of the early atmosphere. *Proc. Natl. Acad. Sci. U.S.A.* 113, 7432–7437.
- Muller, É., Philippot, P., Rollion-Bard, C., Cartigny, P., Assayag, N., Marin-Carbonne, J., Mohan, M.R., Sarma, D.S., 2017. Primary sulfur isotope signatures preserved in high-grade Archean barite deposits of the Sargur Group, Dharwar Craton, India. *Precambrian Res.* 295, 38–47.
- Navarro, M., Tonetto, E., Oliveira, E., 2015. LA-SF-ICP-MS U-Pb Zircon Dating at University of Campinas, Brazil. *Geonalysis-2015*, Wien, August.
- Navarro, M., Tonetto, E., Oliveira, E., 2017. Peixe zircon: new Brazilian reference material for U-Pb geochronology by LA-SF-ICP-MS. *Goldschmidt Conference*, <https://goldschmidtabstracts.info/2017/3815.pdf>.
- Noce, C.M., Zuccheti, M., Baltazar, O., Armstrong, R., Dantas, E., Renger, F.E., Lobato, L., 2005. Age of felsic volcanism and the role of ancient continental crust in the evolution of the Neoproterozoic Rio das Velhas Greenstone belt (Quadrilátero Ferrífero, Brazil): U-Pb zircon dating of volcanoclastic graywackes. *Precambrian Res.* 141, 67–82.
- Ohmoto, H., Watanabe, Y., Ikemi, H., Poulson, S.R., Taylor, B.E., 2006. Sulphur isotope evidence for anoxic Archean atmosphere. *Nature* 442, 908–911.
- Oliver, N.H., Thomson, B., Freitas-Silva, F.H., Holcombe, R.J., Rusk, B., Almeida, B.S., Faure, K., Davidson, G.R., Esper, E.L., Guimarães, P.J., 2015. Local and regional mass transfer during thrusting, veining, and boudinage in the genesis of the giant shale-hosted Paracatu gold deposit, Minas Gerais, Brazil. *Econ. Geol.* 110, 1803–1834.
- Olson, S.L., Kump, L.R., Kasting, J.F., 2013. Quantifying the areal extent and dissolved oxygen concentrations of Archean oxygen oases. *Chem. Geol.* 362, 35–43.
- Ono, S., 2017. Photochemistry of sulfur dioxide and the origin of mass-independent isotope fractionation in earth's atmosphere. *Annu. Rev. Earth Pl. Sci.* 45, 301–329.
- Ono, S., Beukes, N.J., Rumble, D., 2009a. Origin of two distinct multiple-sulfur isotope compositions of pyrite in the 2.5 Ga Klein Naute Formation, Griqualand West Basin, South Africa. *Precambrian Res.* 169, 48–57.
- Ono, S., Beukes, N.J., Rumble, D., Fogel, M.L., 2006a. Early evolution of atmospheric oxygen from multiple-sulfur and carbon isotope records of the 2.9 Ga Mozaan Group of the Pongola Supergroup, Southern Africa. *S. Afr. J. Geol.* 109, 97–108.
- Ono, S., Eigenbrode, J.L., Pavlov, A.A., Kharecha, P., Rumble III, D., Kasting, J.F., Freeman, K.H., 2003. New insights into Archean sulfur cycle from mass-independent sulfur isotope records from the Hamersley Basin, Australia. *Earth Planet. Sci. Lett.* 213, 15–30.
- Ono, S., Kaufman, A.J., Farquhar, J., Sumner, D.Y., Beukes, N.J., 2009b. Lithofacies control on multiple-sulfur isotope records and Neoproterozoic cycles. *Precambrian Res.* 169, 58–67.
- Ono, S., Wing, B., Johnston, D., Farquhar, J., Rumble, D., 2006b. Mass-dependent fractionation of quadruple stable sulfur isotope system as a new tracer of sulfur biogeochemical cycles. *Geochim. Cosmochim. Acta* 70, 2238–2252.
- Papineau, D., Mojzsis, S.J., Schmitt, A.K., 2007. Multiple sulfur isotopes from Paleoproterozoic Huronian interglacial sediments and the rise of atmospheric oxygen. *Earth Planet. Sci. Lett.* 255, 188–212.
- Partin, C., Bekker, A., Planavsky, N., Lyons, T., 2015. Euxinic conditions recorded in the ca. 1.93 Ga Bravo Lake Formation, Nunavut (Canada): implications for oceanic redox evolution. *Chem. Geol.* 417, 148–162.
- Partridge, M.A., Golding, S.D., Baublys, K.A., Young, E., 2008. Pyrite paragenesis and multiple sulfur isotope distribution in late Archean and early Paleoproterozoic Hamersley Basin sediments. *Earth Planet. Sci. Lett.* 272, 41–49.
- Pavlov, A., Kasting, J., 2002. Mass-independent fractionation of sulfur isotopes in Archean sediments: strong evidence for an anoxic Archean atmosphere. *Astrobiology* 2, 27–41.
- Petrus, J.A., Kamber, B.S., 2012. VizualAge: A novel approach to laser ablation ICP-MS U-Pb geochronology data reduction. *Geostand. Geoanal. Res.* 36, 247–270.
- Philippot, P., Ávila, J.N., Killingsworth, B.A., Tessalina, S., Baton, F., Caqueneau, T., Muller, E., Pecoits, E., Cartigny, P., Lalonde, S.V., 2018. Globally asynchronous sulphur isotope signals require re-definition of the Great Oxidation Event. *Nat. Commun.* 9, 1–10.
- Philippot, P., Van Zuilen, M., Lepot, K., Thomazo, C., Farquhar, J., Van Kranendonk, M. J., 2007. Early Archean microorganisms preferred elemental sulfur, not sulfate. *Science* 317, 1534–1537.
- Philippot, P., Van Zuilen, M., Rollion-Bard, C., 2012. Variations in atmospheric sulphur chemistry on early Earth linked to volcanic activity. *Nat. Geosci.* 5, 668–674.
- Planavsky, N., Bekker, A., Rouxel, O.J., Kamber, B., Hofmann, A., Knudsen, A., Lyons, T. W., 2010. Rare earth element and yttrium compositions of Archean and

- Paleoproterozoic Fe formations revisited: new perspectives on the significance and mechanisms of deposition. *Geochim. Cosmochim. Acta* 74, 6387–6405.
- Planavsky, N.J., Robbins, L.J., Kamber, B.S., Schoenberg, R., 2020. Weathering, alteration and reconstructing Earth's oxygenation. *Interface Focus* 10, 20190140. [10.1098/rsfs.20190140](https://doi.org/10.1098/rsfs.20190140).
- Poulton, S., Raiswell, R., 2002. The low-temperature geochemical cycle of iron: from continental fluxes to marine sediment deposition. *Am. J. Sci.* 302, 774–805.
- Poulton, S.W., Canfield, D.E., 2005. Development of a sequential extraction procedure for iron: implications for iron partitioning in continentally derived particulates. *Chem. Geol.* 214, 209–221.
- Poulton, S.W., Canfield, D.E., 2011. Ferruginous conditions: a dominant feature of the ocean through Earth's history. *Elements* 7, 107–112.
- Praharaj, T., Fortin, D., 2004. Determination of acid volatile sulfides and chromium reducible sulfides in Cu-Zn and Au mine tailings. *Water Air Soil Pollut.* 155, 35–50.
- Rahl, J.M., Anderson, K.M., Brandon, M.T., Fassoulas, C., 2005. Raman spectroscopic carbonaceous material thermometry of low-grade metamorphic rocks: calibration and application to tectonic exhumation in Crete, Greece. *Earth Planet. Sci. Lett.* 240, 339–354.
- Raiswell, R., Canfield, D.E., 1998. Sources of iron for pyrite formation in marine sediments. *Am. J. Sci.* 298, 219–245.
- Rantitsch, G., Grogger, W., Teichert, C., Ebner, F., Hofer, C., Maurer, E.-M., Schaffer, B., Toth, M., 2004. Conversion of carbonaceous material to graphite within the Greywacke Zone of the Eastern Alps. *Int. J. Earth Sci.* 93, 959–973.
- Reinhard, C.T., Lalonde, S.V., Lyons, T.W., 2013. Oxidative sulfide dissolution on the early Earth. *Chem. Geol.* 362, 44–55.
- Reinhard, C.T., Raiswell, R., Scott, C., Anbar, A.D., Lyons, T.W., 2009. A late Archean sulfidic sea stimulated by early oxidative weathering of the continents. *Science* 326, 713–716.
- Renger, F.E., Noce, C.M., Romano, A.W., Machado, N., 1994. Evolução sedimentar do Supergrupo Minas: 500 Ma. de registro geológico no Quadrilátero Ferrífero, Minas Gerais, Brasil. *Geonomos*, 10.18285/geonomos.v18282i18281.18227 (in Portuguese).
- Reuschel, M., Melezhik, V., Strauss, H., 2012. Sulfur isotopic trends and iron speciation from the c. 2.0 Ga Pilgūjärvi Sedimentary Formation, NW Russia. *Precambrian Res.* 196, 193–203.
- Ribeiro, Y., e Silva, R.C.F., Lobato, L.M., Lima, L.C., Rios, F.J., Hagemann, S.G., Cliff, J., 2015. Fluid inclusion and sulfur and oxygen isotope studies on quartz-carbonate-sulfide veins of the Carvoaria Velha deposit, Córrego do Sítio gold lineament, Quadrilátero Ferrífero, Minas Gerais, Brazil. *Ore Geol. Rev.* 67, 11–33.
- Ribeiro-Rodrigues, L.C., de Oliveira, C.G., Friedrich, G., 2007. The Archean BIF-hosted Cuibá Gold deposit, Quadrilátero Ferrífero, Minas Gerais, Brazil. *Ore Geol. Rev.* 32, 543–570.
- Riding, R., Fralick, P., Liang, L., 2014. Identification of an Archean marine oxygen oasis. *Precambrian Res.* 251, 232–237.
- Riedinger, N., Formolo, M.J., Lyons, T.W., Henkel, S., Beck, A., Kasten, S., 2014. An inorganic geochemical argument for coupled anaerobic oxidation of methane and iron reduction in marine sediments. *Geobiology* 12, 172–181.
- Roerdink, D.L., Mason, P.R., Whitehouse, M.J., Brouwer, F.M., 2016. Reworking of atmospheric sulfur in a Paleoproterozoic hydrothermal system at Londozi, Barberton Greenstone Belt, Swaziland. *Precambrian Res.* 280, 195–204.
- Roland, F.A., Borges, A.V., Darchambeau, F., Lliros, M., Descy, J.-P., Morana, C., 2021. The possible occurrence of iron-dependent anaerobic methane oxidation in an Archean Ocean analogue. *Sci. Rep.* 11, 1–11.
- Romano, A., 2006. Programa Geologia do Brasil. Folha Pará de Minas SE-23-ZCI. Escala 1: 100.000 relatório final. UFMG-CPRM, Belo Horizonte (in Portuguese).
- Romano, R., Lana, C., Alkmim, F.F., Stevens, G., Armstrong, R., 2013. Stabilization of the southern portion of the São Francisco craton, SE Brazil, through a long-lived period of potassic magmatism. *Precambrian Res.* 224, 143–159.
- Schidlowski, M., 2001. Carbon isotopes as biogeochemical recorders of life over 3.8 Ga of Earth history: evolution of a concept. *Precambrian Res.* 106, 117–134.
- Schirmeister, B.E., Sanchez-Baracaldo, P., Wacey, D., 2016. Cyanobacterial evolution during the Precambrian. *Int. J. Astrobiol.* 15, 187–204.
- Schumann, R., Stewart, W., Miller, S., Kawashima, N., Li, J., Smart, R., 2012. Acid–base accounting assessment of mine wastes using the chromium reducible sulfur method. *Sci. Total Environ.* 424, 289–296.
- Scott, C.T., Bekker, A., Reinhard, C.T., Schnetger, B., Krapež, B., Rumble III, D., Lyons, T. W., 2011. Late Archean euxinic conditions before the rise of atmospheric oxygen. *Geology* 39, 119–122.
- Selvaraja, V., Caruso, S., Fiorentini, M., LaFlamme, C., 2019. The Global Sedimentary Sulfur Isotope Database.
- Selvaraja, V., Caruso, S., Fiorentini, M.L., LaFlamme, C.K., Bui, T.-H., 2017. Atmospheric sulfur in the orogenic gold deposits of the Archean Yilgarn Craton, Australia. *Geology* 45, 691–694.
- Siebert, C., Kramers, J., Meisel, T., Morel, P., Nägler, T.F., 2005. PGE, Re-Os, and Mo isotope systematics in Archean and early Proterozoic sedimentary systems as proxies for redox conditions of the early Earth. *Geochim. Cosmochim. Acta* 69, 1787–1801.
- Sivan, O., Adler, M., Pearson, A., Gelman, F., Bar-Or, I., John, S.G., Eckert, W., 2011. Geochemical evidence for iron-mediated anaerobic oxidation of methane. *Limnol. Oceanogr.* 56, 1536–1544.
- Slotznick, S.P., Eiler, J.M., Fischer, W.W., 2018. The effects of metamorphism on iron mineralogy and the iron speciation redox proxy. *Geochim. Cosmochim. Acta* 224, 96–115.
- Steadman, J., Large, R., Blamey, N., Mukherjee, I., Corkrey, R., Danyushevsky, L., Maslennikov, V., Hollings, P., Garven, G., Brand, U., 2020. Evidence for elevated and variable atmospheric oxygen in the Precambrian. *Precambrian Res.* 343, 105722. [10.1016/j.precamres.2020.105722](https://doi.org/10.1016/j.precamres.2020.105722).
- Stüeken, E.E., Buick, R., Lyons, T.W., 2019. Revisiting the depositional environment of the Neoproterozoic Callanna Group, South Australia. *Precambrian Res.* 334, 105474. [10.1016/j.precamres.2020.105474](https://doi.org/10.1016/j.precamres.2020.105474).
- Stüeken, E.E., Catling, D.C., Buick, R., 2012. Contributions to late Archean sulphur cycling by life on land. *Nat. Geosci.* 5, 722–725.
- Tedeschi, M., Hagemann, S.G., Roberts, M.P., Evans, N.J., 2018. The Karouni Gold Deposit, Guyana, South America: Part II. Hydrothermal alteration and mineralization. *Econ. Geol.* 113, 1705–1732.
- Teixeira, W., Ávila, C., Dussin, I., Neto, A.C., Bongioio, E., Santos, J., Barbosa, N., 2015. A juvenile accretion episode (2.35–2.32 Ga) in the Mineiro belt and its role to the Minas accretionary orogeny: Zircon U-Pb-Hf and geochemical evidences. *Precambrian Res.* 256, 148–169.
- Thomazo, C., Ader, M., Farquhar, J., Philippot, P., 2009a. Methanotrophs regulated atmospheric sulfur isotope anomalies during the Mesoproterozoic (Tumbiana Formation, Western Australia). *Earth Planet. Sci. Lett.* 279, 65–75.
- Thomazo, C., Nisbet, E.G., Grassineau, N.V., Peters, M., Strauss, H., 2013. Multiple sulfur and carbon isotope composition of sediments from the Belingwe Greenstone Belt (Zimbabwe): A biogenic methane regulation on mass independent fractionation of sulfur during the Neoproterozoic? *Geochim. Cosmochim. Acta* 121, 120–138.
- Thomazo, C., Pinti, D.L., Busigny, V., Ader, M., Hashizume, K., Philippot, P., 2009b. Biological activity and the Earth's surface evolution: insights from carbon, sulfur, nitrogen and iron stable isotopes in the rock record. *C. R. Palevol* 8, 665–678.
- Tuinstra, F., Koenig, J.L., 1970. Raman spectrum of graphite. *J. Chem. Phys.* 53, 1126–1130.
- Ueno, Y., 2014. Coping with low ocean sulfate. *Science* 346, 703–704.
- Ueno, Y., Yamada, K., Yoshida, N., Maruyama, S., Isozaki, Y., 2006. Evidence from fluid inclusions for microbial methanogenesis in the early Archean era. *Nature* 440, 516–519.
- Verma, S.K., Oliveira, E.P., Silva, P.M., Moreno, J.A., Amaral, W.S., 2017. Geochemistry of komatiites and basalts from the Rio das Velhas and Pitangui greenstone belts, São Francisco Craton, Brazil: Implications for the origin, evolution, and tectonic setting. *Lithos* 284, 560–577.
- Vial, D., Abreu, G., Schubert, G., Ribeiro-Rodrigues, L., 2007. Smaller gold deposits in the Archean Rio das Velhas greenstone belt, Quadrilátero Ferrífero, Brazil. *Ore Geol. Rev.* 32, 651–673.
- Wang, Y., Hندی, I.L., Latimer, J.C., Bilardello, D., 2019. Diagenesis and iron paleoredox proxies: New perspectives from magnetic and iron speciation analyses in the Santa Barbara Basin. *Chem. Geol.* 519, 95–109.
- Wiedenbeck, M., Alle, P., Corfu, F., Griffin, W., Meier, M., Oberli, F.V., Quadt, A.V., Roddick, J., Spiegel, W., 1995. Three natural zircon standards for U-Th-Pb, Lu-Hf, trace element and REE analyses. *Geostand. Newsletter* 19, 1–23.
- Williford, K.H., Ushikubo, T., Lepot, K., Kitajima, K., Hallmann, C., Spicuzza, M.J., Kozdon, R., Eigenbrode, J.L., Summons, R.E., Valley, J.W., 2016. Carbon and sulfur isotopic signatures of ancient life and environment at the microbial scale: Neoproterozoic shales and carbonates. *Geobiology* 14, 105–128.
- Wit, D., 1998. Vaalbara, Earth's oldest assembled continent? a combined structural, geochronological, and palaeomagnetic test. *Terra Nova* 10, 250–259.
- Wu, L., Beard, B.L., Roden, E.E., Johnson, C.M., 2009. Influence of pH and dissolved Si on Fe isotope fractionation during dissimilatory microbial reduction of hematite. *Geochim. Cosmochim. Acta* 73, 5584–5599.
- Xue, Y., Campbell, I., Ireland, T.R., Holden, P., Armstrong, R., 2013. No mass-independent sulfur isotope fractionation in auriferous fluids supports a magmatic origin for Archean gold deposits. *Geology* 41, 791–794.
- Zahnle, K., Claire, M., Catling, D., 2006. The loss of mass-independent fractionation in sulfur due to a Paleoproterozoic collapse of atmospheric methane. *Geobiology* 4, 271–283.
- Zerkle, A.L., Claire, M.W., Domagal-Goldman, S.D., Farquhar, J., Poulton, S.W., 2012. A bistable organic-rich atmosphere on the Neoproterozoic Earth. *Nat. Geosci.* 5, 359–363.
- Zhang, Y., Gao, J.-F., Ma, D., Pan, J., 2018. The role of hydrothermal alteration in tungsten mineralization at the Dahutang tungsten deposit, South China. *Ore Geol. Rev.* 95, 1008–1027.
- Zhelezinskaja, I., Kaufman, A.J., Farquhar, J., Cliff, J., 2014. Large sulfur isotope fractionations associated with Neoproterozoic microbial sulfate reduction. *Science* 346, 742–744.